7-24-2012

Tensile Testing of Polyurea Crosslinked Silica Aerogel Impregnated Silicone and Amine Functionalized Polyoligomeric Silsesquioxane Crosslinked Polyimide Aerogel for Cryogenic Tank Applications.

K M Rifat Faysal

TENSILE TESTING OF POLYUREA CROSSLINKED SILICA AEROGEL IMPREGNATED SILICONE AND AMINE FUNCTIONALIZED POLYOLIGOMERIC SILSESQUIOXANE CROSSLINKED POLYIMIDE AEROGEL FOR CRYOGENIC TANK APPLICATIONS

by

K. M. Rifat Faysal

A Thesis

Submitted in Partial Fulfillment of the

Requirement for the Degree of

Master of Science

Major: Physics

The University of Memphis

August 2012

DEDICATION

To my Mother….

ACKNOWLEDGEMENTS

First of all my special thanks go to Dr. Firouzeh Sabri, Dr.Jeffrey G Marchetta, and Dr. John W Hanneken for mentoring, guiding, and helping me over the past two years. Author would like to thank John Daffron from the Department of Physics Instrument Shop as well as Rick and Robert from the engineering machine shop at the University of Memphis. My special thanks also go to Charles Nathan Melton, Andrew Brock, and Chris Hatch for helping and encouraging me throughout the last two years. The author also would like to acknowledge financial support from NASA TN EPSCOR NNX10AQ71A.

ABSTRACT

Faysal, K. M. Rifat. M.S. The University of Memphis. August/2012. Tensile Testing of Polyurea Crosslinked Silica Aerogel Impregnated Silicone and Amine Functionalized Polyoligemeric Silsesquioxane Polyimide Aerogel for Cryogenic Tank Applications. Major Professor: Firouzeh Sabri, Ph.D.

Polymer-based thermally insulating vessels are an attractive option for future space exploratory missions as well as for the energy conserving terrestrial applications as an alternative to the conventional metal-based structures. Aerogel due to its unique set of material properties, such as superior thermal insulation and light weight, makes it an attractive for future space applications. Room Temperature (RT) and Low Temperature (LT) evaluation of the mechanical properties of Polyurea Crosslinked Silica Aerogel (PCSA) impregnated RTV 655 was performed under increasing concentrations of PCSA. The effect of PCSA particles sizes on the tensile behavior of RTV 655 was also assessed and compared with the tensile behavior of neat RTV 655 at both RT and LT. Incorporated PCSA particles ranges were varied from 90-425μm and the concentrations tested were 25%, 50%, and 75% weight to the RTV 655. The tensile properties of amine functionalized Polyoligomeric Silsesquioxane (POSS) crosslinked Polyimide (PI) aerogel strips were also evaluated at both RT and LT and the effect of the geometry and flexibility of PI-based aerogels was compared with the results obtained from PCSA impregnated RTV 655 samples.

TABLE OF CONTENTS

LIST OF TABLES

LIST OF FIGURES

LIST OF SYMBOLS AND ABBREVIATIONS

Chapter 1

INTRODUCTION

1.1 IntroductiontoAerogels:

Aerogels are the lightest known solid on earth[1]. Aerogel was not commercialized until the 1950's, in spite of its invention in 1931 by Samuel Stephens Kistler[1]. Its very high surface area to volume ratio and very low thermal conductivity due to its nano-porous nature has drawn the attention of both materials scientists and engineers. While crosslinked aerogels overcame with the fragility issue of native aerogels[1], the stiffness attribute of this category has created limitations on the applications window.

Silica aerogel is the most studied type of aerogel and have been utilized for a variety of space-related missions such as insulation on the Mars exploration rovers[3], hypervelocity particle capture in the Stardust probe[4], high energy Cerenkov radiation particle counter [5], and other applications such as remediating oil from water[6], and window insulation. The fragility of native silica aerogel[1,7] has limited its utilization in many applications. This shortcoming has been addressed in recent years by mechanically reinforcing the silica chains and creating "crosslinked" aerogel[7-10] which has been the focus of the work presented here.

1.2 Effect of "doping" on mechanical behavior of polymers:

Many studies have been conducted to modify the mechanical properties of polymers by incorporating a few weight (wt.) percentages of foreign elements in order to cope with the inherent material limitations, such as low stiffness, low (yield) strength, and low load bearing capabilities to name a few. The mechanical strength of any composite strongly depends on the stress transfer between the incorporated particles and

the matrix which is of course related to the particle geometry and size as well as the nature of the interaction between the polymer and the foreign elements. It has been shown in many studies that for chemically well-bonded constituent particles, the applied stress can be effectively transferred to the incorporated elements from the matrix[11]. This clearly improves the overall strength[12-16] whereas the incorporation with the poorly bonded micro-particles, the overall strength of the matrix decreases[17-25]. Several studies have reported the trend of an increase in the fracture toughness of the thermoplastic composites filled with rigid particulates as compared to the neat polymers[25-27]. Most of the investigations have reported a significant amount of lessening in the fracture toughness of the composites due to the introduction of foreign elements[19,28,29]. On the other hand, thermosetting resins are found to have poor resistance to crack growth and propagation[19,30,31]. It is therefore clear that the mechanical properties of both thermoset (a polymer that irreversibly cures) and thermoplastic (a polymer that reversible cures) can be modified by adding varying concentrations and sizes of embedded components[18,19,32-35].

1.3 Motivation and Focus of this work:

Polyurea Crosslinked Silica Aerogel (PCSA) is naturally rigid in nature and cannot be easily molded into complex geometries. Despite the rigid nature of crosslinked silica aerogel, it is possible to take the advantage of its unique properties by incorporating it in the form of beads, particles, or capsules into a pliable matrix. Incorporation into a polymer matrix could enhance the thermal insulation properties of the base polymer by several orders. For example, encapsulating the PCSA into a pliable elastomer could create a structure with the excellent thermal insulation properties as well as maintaining

the geometrical conformability. The exact effect of PCSA incorporation into the elastomeric matrix on the mechanical properties is yet unknown and needs to be fully investigated. It has been already proven that incorporation of native aerogel beads into a thermoplastic material could reduce the thermal conductivity significantly [1,36]. So introduction of PCSA into elastomeric matrix for example, RTV 655: a space graded elastomer could also reduce the thermal conductivity of the compound material. But the change in the mechanical properties of this proposed RTV-PCSA compound material is yet unknown and will be addressed herein. Therefore it is necessary to understand how the aforementioned parameters like incorporation particle sizes, concentrations, geometries could modify the mechanical properties of the compound material.

An alternative approach could also be carried out by incorporating a flexible type aerogel in the form of strips instead of rigid PCSA such as amine functionalized Polyoligomeric Silsesquioxane (POSS) crosslinked Polyimide (PI) aerogel[37]. This particular type can be folded and cured in the form of thin sheets which appears to be promising for the future applications as a conformable insulator. In this study, the mechanical properties of PI aerogel have been investigated as an alternative material.

Room temperature vulcanizing rubbers such as RTV 655 have been utilized extensively in the space applications such as on board Mars Pathfinder, the Mars rovers, and the Phoenix Lander. RTV 655 is a space qualified polymer which is capable of retaining its flexibility over the wide range of temperatures [38,39] as well as could provide good thermal insulation. In this work, both PCSA particles of varying sizes and concentrations and PI have been incorporated into RTV 655 matrix and the effect of concentrations, sizes, and geometry of two kinds of aerogels on the mechanical behavior

of RTV 655 has been investigated. The investigation was carried out on the RTV-PCSA compound material with the three varying PCSA particle sizes of 425-300μm, 300-180μm, and 180-90μm at increasing concentrations of 25%, 50%, and 75% weights (wt.) to the neat polymer. Measurements were performed at both room temperature (293K) and at low temperature (77K). The tensile behavior of neat amine functionalized POSS crosslinked PI aerogel as well as RTV-PI compound specimens were also assessed at 293K and 77K. The POSS crosslinked PI embedding concentrations were 22%, 39%, and 56% volume to the RTV 655.

1.4 Organization of the thesis:

In Chapter 2 the theoretical background of all the scientific instruments utilized for this study has been reviewed as well as the corresponding formulas to calculate the weight fractions, area fractions, and volume fractions has been provided. Chapter 3 describes the synthesis steps followed to prepare both the PCSA as well as amine functionalized POSS crosslinked PI aerogel. Detailed steps for synthesis of compound samples are also presented in this chapter. In Chapter 4 the tensile testing system has been introduced and the setup utilized to perform the room temperature and low temperature tests is described in detail. The effect of the impregnation of RTV 655 with PCSA micro-particles and PI strips on the tensile behavior is presented in Chapter 5 along with other supporting characterizations data. Finally, conclusions and suggestions for further work are presented in Chapter 6.

Chapter 2

THEORETICAL BACKGROUND

The most relevant fundamental theories regarding tensile testing as it relates to pressurized cylindrical vessels will be discussed in this Chapter. Moreover, some of the sections of this chapter will contain theories regarding the working principles of various types of scientific instruments that have been utilized to prepare and characterize component materials. Descriptions on working principles of supercritical point drier, nitrogen adsorption machine, scanning electron microscope, UV-VIS spectrophotometer will also be provided. A section will also present the mathematical formulas used in this study to calculate parameters such as bulk density, weight fraction, volume fraction, and area fraction.

2.1 Introduction to mechanical testing of materials:

There are various types of tests that can determine the mechanical properties of a material such as tensile testing, compression testing, materials hardness testing, material impact testing, and three point bending. The selection among the aforementioned test types could be very important and depend on applications. As a subdivision of a project the feasibility of polymer-based compound materials as a prospective structural material for a pressurized cryogenic propellant tank has been carried out. Hence the fundamental theory relating to cylindrical pressure vessel will be discussed in the section.

The most common form of geometry for a pressurized vessel is a cylindrical shape. Any enclosed pressurized vessels usually are subject to constant outward pressure which could lead the system to various types of failures such as elastic deformation, stress rupture, plastic instability, and brittle fracture[41]. In general, the cylindrical

pressurized vessel is subject to axis symmetric loading and deformation which can be divided into three components of forces: axial force, tangential force and radial force[42-44]. The wall of a tank or pipe carrying a fluid under pressure is subjected to the tensile or axial forces across its longitudinal and transverse sections. The circumferential force, also known as tangential force, in a tank or pipe can be determined by applying the concept of fluid pressure against curved surfaces. Finally the radial force tends to change the wall thickness. A simplified diagram (Figure 2.1) will help to picture the acting forces on an enclosed pressurized vessel. Now the mathematical treatments for these three types of stresses will be provided here[41-44].

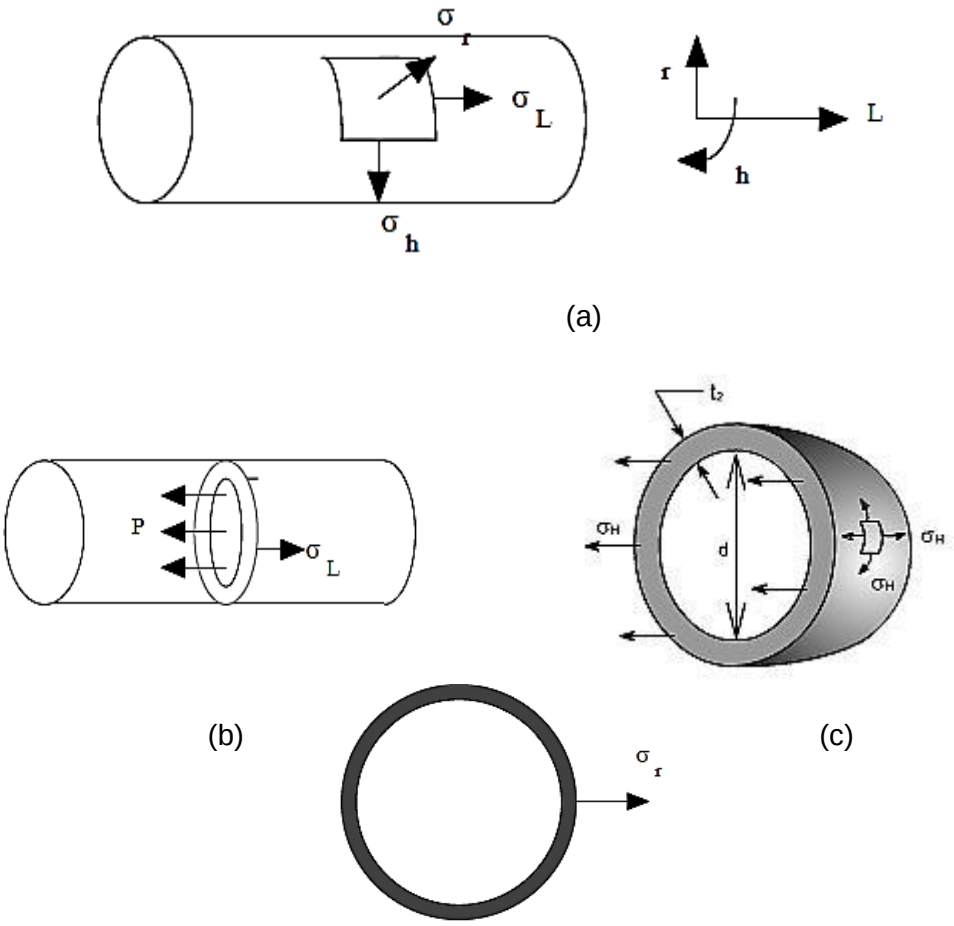

Figure 2.1: Three types of stresses that act on any pressurized cylindrical vessel. (a) stress components acting on an infinitesimal segment on the wall, (b) axial stress or tensile stress, (c) hoop stress, and (d) radial stress.

Longitudinal stress:

At the force equilibrium

$$\frac{\pi D^2}{4}(P) = \pi D t \sigma_L \quad (1)$$

where, D, and t are the diameter, thickness of the cylinder, and P, and σ_L are the internal outward pressure, and tangential stress acting on the cylindrical vessel. If P>0, then σ_L is tensile and can be expressed as:

$$\sigma_L = \frac{PD}{4t} \quad (2)$$

Hoop stress:

Again, at force equilibrium

$$DLP = 2\sigma_h L t \quad (3)$$

$$\sigma_h = \frac{PD}{2t} \quad (4)$$

Radial stress:

Radial stress σ_r can vary from P on the inner face to zero on the outer face. For a thin wall cylindrical vessel, it essentially can be neglected. Therefore, only tensile stress and circumference stress or hoop stress are active on a thin wall cylindrical pressurized

vessel. Now the net stress can be written in a matrix form with the help of cylindrical coordinates (r, θ, x) as follows:

$$\sigma = \begin{bmatrix} \sigma_{rr} & \sigma_{r\theta} & \sigma_{rx} \\ \sigma_{r\theta} & \sigma_{\theta\theta} & \sigma_{\theta x} \\ \sigma_{rx} & \sigma_{\theta x} & \sigma_{xx} \end{bmatrix} = \begin{bmatrix} 0 & 0 & 0 \\ 0 & \frac{Pr}{t} & 0 \\ 0 & 0 & \frac{Pr}{2t} \end{bmatrix} \quad (5)$$

where, r is the radius of the cylinder.

The aforementioned stresses also can deform the subjugated material towards the direction of respective forces. Hence, fractional changes in dimensions can be referred as three different strains: axial strain, hoop strain, and radial strain[41-45].

These strains can be correlated with their corresponding stresses as follows:

$$\varepsilon_l = \frac{1}{E}[\sigma_{xx} - \vartheta(\sigma_{rr} + \sigma_{\theta\theta})] + \alpha\Delta T \quad (6)$$

$$\varepsilon_h = \frac{1}{E}[\sigma_{\theta\theta} - \vartheta(\sigma_{rr} + \sigma_{xx})] + \alpha\Delta T \quad (7)$$

$$\varepsilon_r = \frac{1}{E}[\sigma_{rr} - \vartheta(\sigma_{xx} + \sigma_{\theta\theta})] + \alpha\Delta T \quad (8)$$

where E, υ, α, and ΔT are modulus of elasticity, Poisson ratio, coefficient of expansion and temperature, respectively.

By now it is conspicuous that tensile stress is one of the component stresses acting on pressurized cylindrical vessel and hoop stress is nothing but two times greater than the tensile stress. Moreover, for thin wall cylinders, radial stress can be neglected. Therefore,

as a preliminary investigation, studying the tensile properties for the proposed polymer-based composite is found to be the most relevant type of mechanical characterization. Properties that can be determined from such an experiment are Young's modulus, stress to failure, strain to failure, modulus of toughness, modulus of elasticity, resilience, yield stress, and ultimate tensile stress. Aforementioned parameters can be readily calculated from the stress-strain profile of the testing specimen.

2.2 Stress vs. Strain Profile:

Stress is defined as force per unit cross-sectional area. But the cross-sectional area may change if the material deforms due to the stretching. So when the area used in the calculation is the original non-deformed cross-sectional area then the corresponding stress is referred to as engineering stress. On the other hand, true stress is defined as the ratio of the applied load to the instantaneous cross-sectional area[46].

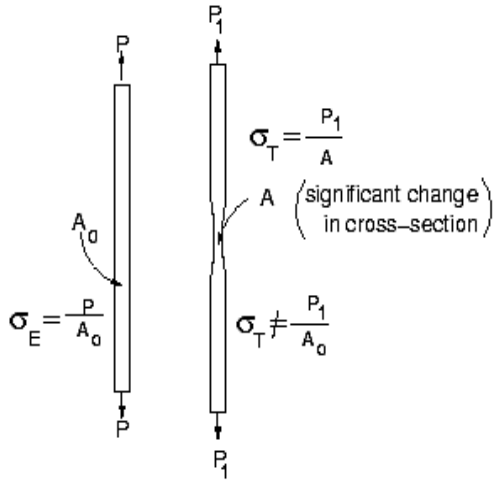

Figure 2.2: Engineering stress vs. true stress.

Strain which is a deformation due to the applied external force can also be divided into two: engineering strain and true strain. Engineering strain takes into account the fixed reference quantities i.e. the initial length of the specimen. On the other hand, the true strain is defined as the sum of all the instantaneous engineering strains. For our experimental result, the engineering stress and strain will be measured. The tensile profile obtained from any tensile experiment could vary depending upon the materials type as well as testing conditions. Typical tensile profiles for various types of polymers and the effect of temperature on these tensile profiles are shown in Figure 2.3[47].

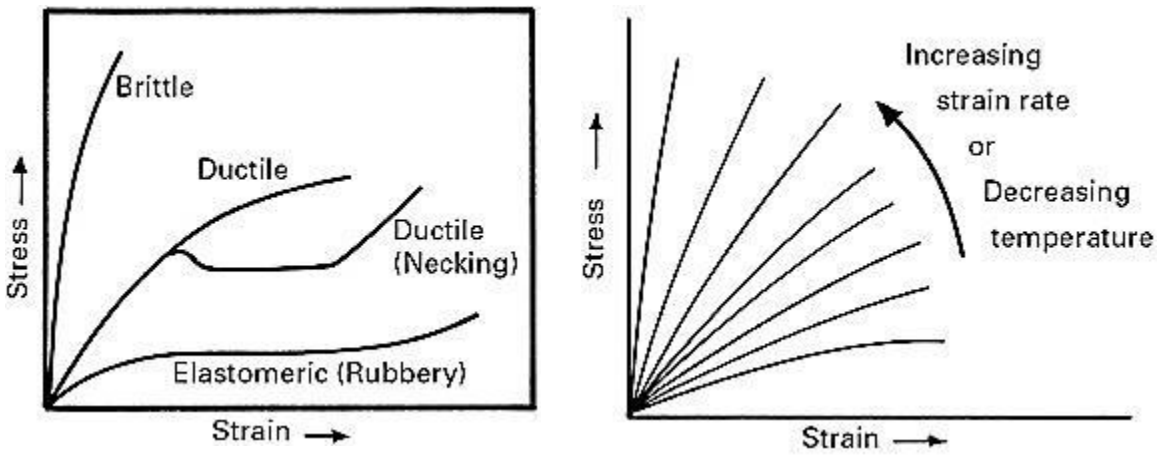

Figure 2.3: (a) Schematic of the different types of stress strain curves in a polymer, and (b) Effect of strain rate and temperature on stress strain curves.

From Figure 2.3a it can be seen that brittle polymers rupture at higher stress but lower strain compared to the elastomers. Moreover, the role of temperature on the mechanical properties of polymer is substantial (Figure 2.3b). As the temperature decreases, the stress vs. strain profile of certain polymers shifts towards the brittle profile. Figure 2.3 also signifies the effect of strain rate on the tensile profile of a specific material which will be discussed later. A particular focus will be provided on the elastomeric tensile profile because one of component materials of the proposed matrix is RTV 655 which falls into the category of thermoset elastomer.

As mentioned beforehand various types of parameters can be obtained from a typical tensile profile. A typical tensile profile of both the thermoplastic materials and thermoset elastomeric materials are presented in Figure 2.4[49-51]. Various terminologies that are shown in Figure 2.4a can be summarized as follows (Table 1) for convenience.

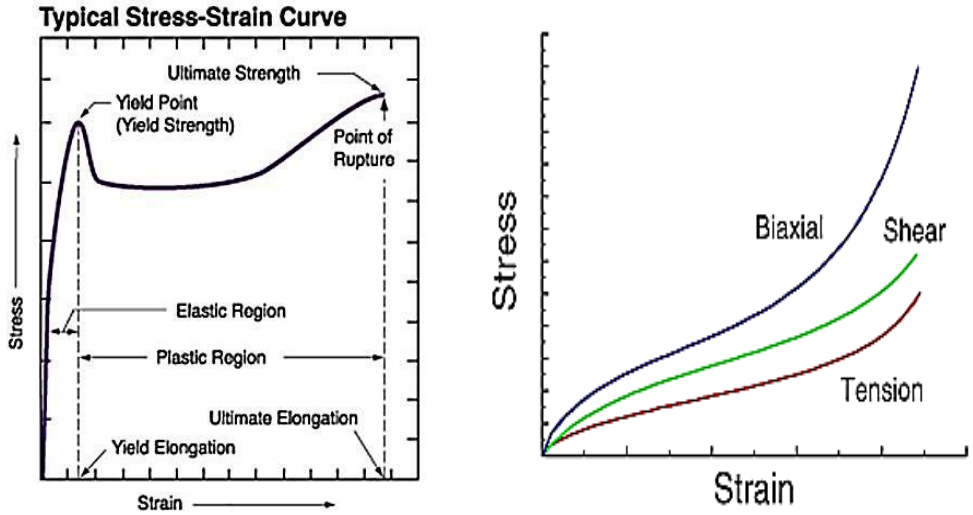

(a) (b)

Figure 2.4: (a) Typical tensile profile of a thermoplastic polymer and (b) typical tensile profile of thermoset polymer obtained by means of different set of mechanical tests.

Table 1 Definitions of various tensile parameters

Definition	Description
Yield Point	It is the stress corresponding to the intersection of the stress-strain curve. Usually by drawing a line parallel to its straight line portion offset by a specified strain e.g. 0.2% for metals. This is when the specimen's cross-sectional area begins to decrease. This is called necking.
Young’s modulus	The ratio of stress to strain within the elastic region of the stress-strain curve.
Yield Elongation	The strain at the yield point.
Elastic Region	The portion of the curve before the yield point.
Plastic Region	The portion of the curve after the yield point.
Ultimate Tensile Strength (UTS)	Ultimate tensile strength is the maximum stress a material can withstand before failing.
Ultimate elongation	The total elongation just before fracture
Tensile Strength	Point of fracture

Figure 2.4b represents the typical tensile behavior of an elastomeric material (red profile) obtained from a uniaxial tensile test. This type of profile is usually known as “S” curve and can be modeled with the help of sigmoidal function which essentially possesses two tangents at two points (Figure 2.4b); the first tangent represents the phenomenon called the necking. The second tangent implies the drawing of materials into the neck region from the outside of the neck region when stress begins to rise uniformly until eventually ruptures occurs. Finally the overall tensile nature of a material can be pictured with the help of presented Figure 2.5. Notice that, this is not an exact tensile profile but an overall slope of the profile.

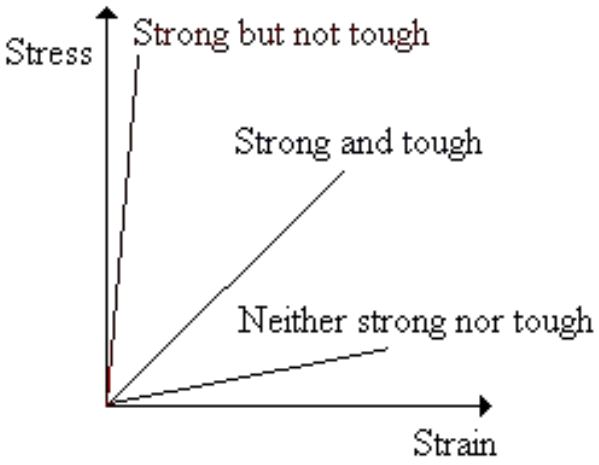

Figure 2.5: Prediction of mechanical nature based on tensile profile slope.

2.3 Introduction to supercritical fluids and Critical point drying:

Critical point drying is a technique to remove the liquid from a material in a controlled way. It is so named because as part of its process, the phenomenon known as the continuity of state occurs, where there is no apparent difference between the liquid and gas state of an element (Figure 6). The surface tension between these interfaces essentially reduces to zero. This occurs at a specific temperature and pressure and is known as the critical point. For CO2, this temperature and pressure are approximately 31.50C and 1072psi. This condition of zero surface tension was used to dry PCSA sol-gel in order to avoid the damaging effects of surface tension. The phase diagram shows the pressure to temperature ranges where solid, liquid and vapor exist. Along the boundary between the liquid and vapor phases, it is possible to choose a particular temperature and corresponding pressure, where liquid and vapor can co-exist and hence have the same density. A critical point drier relies on this physical principle.

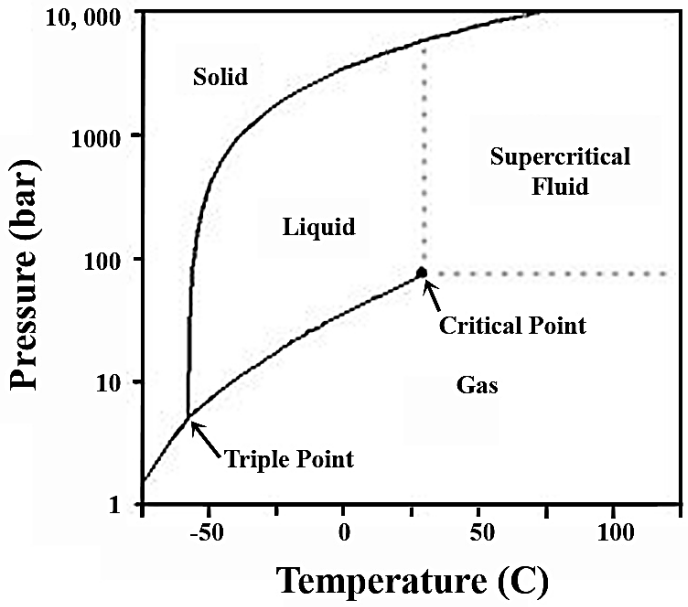

Figure 2.6: Phase diagram of CO_2.

2.4 Review of Gas adsorption Techniques and Porosimetry:

Adsorption means the attachment of molecules to the surface of a solid. In contrast, absorption means the dissolution of molecules within a collecting medium, which may be liquid or solid. The phenomenon of adsorption can be classified into two types: physisorption and chemisorption. Adsorption is mainly caused due to the Van der Waals and electrostatic forces between the adsorbate molecules and the adsorbent surface. Therefore the surface properties such as surface area, polarity and pore size distribution can be evaluated by means of this phenomenon. Scientists over the years developed various models to analyze surface area, pore size, and pore volume. Figure 2.7 explains the physisorption process in accordance with different adsorption theories.

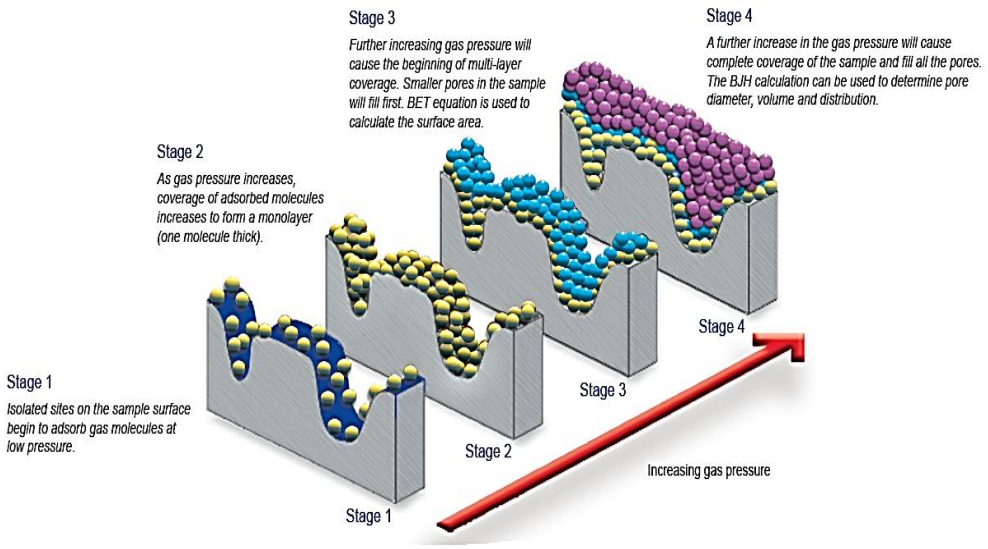

Figure 2.7: Gas adsorption working principles.

Table 2 presents some of the models in a succinct form that have been utilized to measure aforementioned parameters.

Table 2 Summary of commonly used gas adsorption models

Model	Main assumptions	Applications
Langmuir	• The surface of the adsorbent is uniform. • Adsorbed molecules do not interact. • At the maximum adsorption, only a monolayer is formed.	Determines surface area based on monolayer coverage of the specimen.
BET	• Often molecules do form multilayer • The successive heats of adsorption for all layers except the first are equal to the heat of condensation of the adsorbate.	To determine surface area, pore size, pore volume, pore density. in a nanometer scale based on a model of adsorption which incorporates multilayer coverage. The most utilized model by the scientific community.
BJH	• Calculate the pore size distributions from experimental isotherms using the Kelvin model of pore filling.	It applies only to the mesopore and small macropore size range.
deBOER t-plot	• It is based on standard isotherms and thickness curves which describe the standard t-plot.	Most commonly used to determine the external surface area and micropore volume of microporous materials.
DFT	• Density functional theory provides a method by which the total expanse of the experimental isotherm can be analyzed to determine.	Both microporosity and mesoporosity in a continuous distribution of pore volume in respect to pore size.
Horvath-Kawazoe Technique	• The original H-K method is based on slit-shaped pores.	Micropore volume.

It is obvious that there are many models available to analyze surface properties or measure the pore density and volume. However, only the theoretical aspects of the Brunauer, Emmett and Teller (BET) model (1938) will be provided. The BET method can be used to determine the pore volume, pore density, surface area, and pore diameter of the aerogel at a nanometer scale. In contrast to the Langmuir model, the BET model accounts for multilayer adsorption and the dependency of the adsorption enthalpy, ΔH on surface. The BET model is based on the following formula:

$$\frac{x}{v(1-x)} = \frac{1}{cv_{mon}} + \frac{x(c-1)}{cv_{mon}} \tag{9}$$

where x is the pressure divided by the vapor pressure for the adsorbate at a specific temperature, v is the STP volume of adsorbed adsorbate, v_{mon} is the STP volume of the amount of adsorbate required to form a monolayer and c is the equilibrium. Usually these parameters are obtained from isotherms of the adsorbates.

2.5 Review of scanning electron microscopy technique:

A scanning electron microscope utilizes electron waves instead of light waves to form an image at a molecular level. The conventional microscope is limited by the visible range of the wavelength whereas a scanning electron microscope can scan at a nanometer scale due to the very short de Broglie wave of electrons. Figure 2.8 explain the working mechanism of a scanning electron microscope. The accelerated electron beam emitted from the electron gun passes through anode and magnetic lens and bounces off the

examined specimen and collected by a detector and processed further to obtain a sharp image at the molecular level.

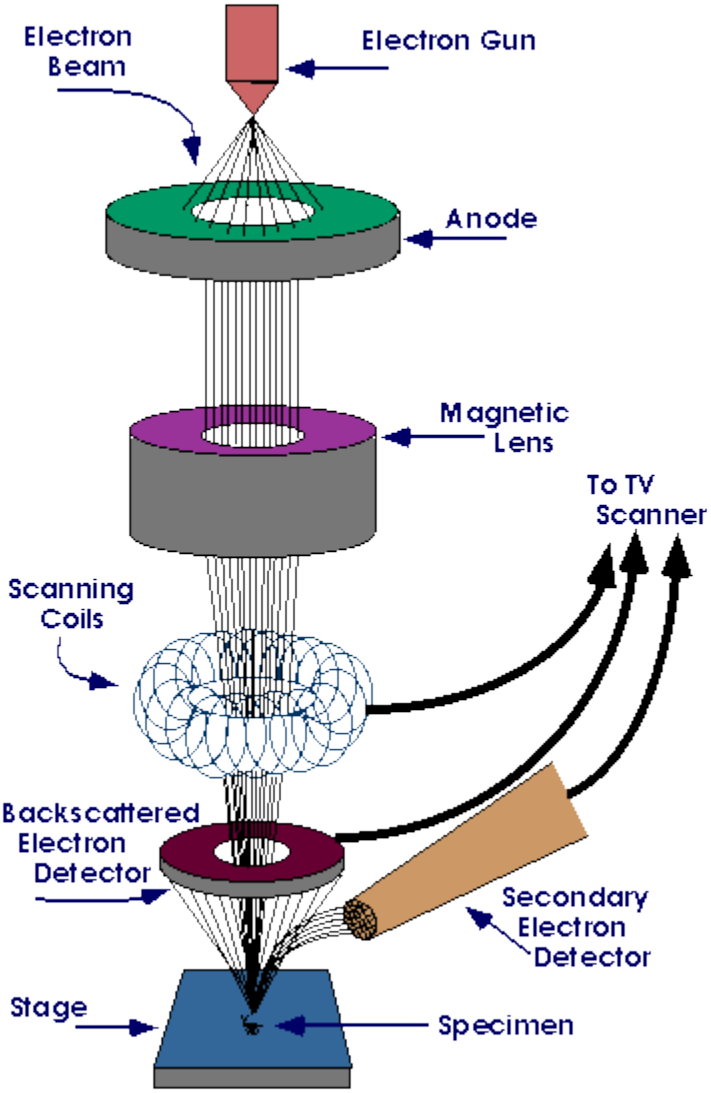

Figure 2.8: Schematic diagram of scanning electron microscopy technique.

Accelerated electrons normally carry a significant amount of kinetic energy, and this energy is dissipated by electron-sample interactions as the incident electrons are decelerated as it bounces off the solid sample. These signals include secondary electrons (that produce the SEM images), backscattered electrons (BSE), and characteristic X-rays. Secondary electrons and backscattered electrons are commonly used for imaging a sample. Secondary electrons are the most valuable for showing morphology and topography of the examined samples and backscattered electrons are the most valuable for illustrating the contrasts in multiphase samples.

2.6 Review of spectrophotometry:

A UV-VIS spectrophotometer or ultraviolet visible spectrophotometer is a scientific tool to characterize a solution or samples optically. This is mainly used to determine the absorbance profile of a chemical solution. The working principle is very straight forward. First, a light source generates light at a specific wavelength or wavelengths. Commonly, UV-VIS spectrophotometers utilize two light sources: a deuterium arc lamp for consistent intensity in the UV range (190 to 380 nm) and a tungsten-halogen lamp for consistent intensity in the visible spectrum (380 to about 800 nm). Some spectrophotometers also use xenon flash lamps which offer decent intensity over the UV and visible regions. The source light is then directed to a dispersion device that causes different wavelengths of light to be dispersed at different angles. The most common dispersion device used is a prism. As the beam hits the prism, it disperses into different wavelength and only a specific wavelength is allowed to pass through the exit slit (Figure 2.9). Finally the beam of any particular wavelength impinges on the detector. Photomultipliers or diodes are usually widely used as a detector. The detector determines

the absorbance or transmittance coefficient by means of further processing. The Beer-Lambert law is associated with this working principle of spectrophotometer and is given below:

$$\boldsymbol{A = \alpha_{\lambda} * b * c} \tag{10}$$

where A is the measured absorbance,$\boldsymbol{\alpha_{\lambda}}$is wavelength dependent absorptivity coefficient, b is the path length, and c concentration of the solution.

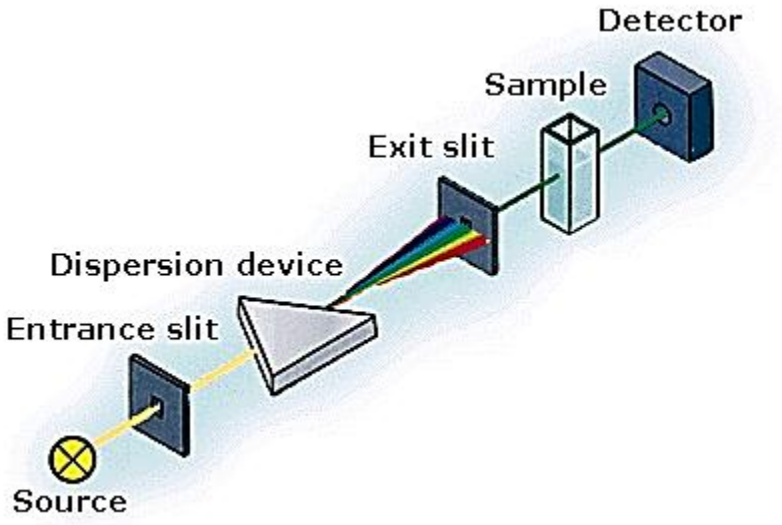

Figure 2.9: Working principle of a UV-VIS spectrophotometer.

2.7 Calculation of weight and volume percentages of PCSA- impregnated RTV 655 samples:

The following simple formula has been used to calculate the weight (wt.) fraction of the aerogel to the neat polymer (RTV 655).

$$wt.(\%) = \frac{wt._{aerogel}}{wt._{aerogel} + wt._{RTV655}} \times 100 \quad (11)$$

Although the prepared testing samples were based on the above calculation, the weight fraction could readily be converted into volume fractions using the following formula:

$$V(\%) = \frac{V_{aerogel}}{V_{aerogel} + V_{RTV655}} \times 100 \quad (12)$$

$$V(\%) = \frac{\frac{m_{aerogel}}{\rho_{aerogel}}}{\frac{m_{aerogel}}{\rho_{aerogel}} + \frac{m_{RTV\ 655}}{\rho_{RTV\ 655}}} \times 100 \quad (13)$$

where $m_{aerogel}$, and $m_{RTV\ 655}$, are the mass of aerogel and RTV 655 and $\rho_{aerogel}$, and $\rho_{RTV\ 655}$ are the density of aerogel and RTV 655.

2.8 Calculation of cross-sectional area fraction of RTV-PI:

The following formula has been used to calculate the cross-sectional area fraction of PI strip to the neat polymer-

$$A(\%) = \frac{A_{PI}}{A_{PI}+A_{RTV\ 655}} \times 100 \quad (14)$$

where A represents the area of the corresponding subscripts which is Polyimide (PI) and RTV 655.

Chapter 3

SYNTHESIS AND SAMPLE PREPARATION

3.1 Synthesis of polyurea crosslinked silica aerogel:

Native sol-gels were synthesized in the form of cylindrical monoliths, and cross-linked with isocyanate in accordance with previously published work[1,2]. The synthesis was carried out in several batches with each batch consisting of ten monoliths.

Tetramethoxysilane, 3 aminopropylsilane and acetonitrile were purchased from Sigma Aldrich (Milwaukee, WI) and used as received. Methanol and deionized (DI) water were acquired from Fisher Scientific Inc. DESMADUR was purchased from Bayer Corporation (Pittsburg, PA). The first step was to measure the chemicals very carefully as mentioned below. A 4.25 mL volume of methanol in a 10mL cylinder (cylinder A), a 3.85 mL volume of TMOS in another 10 mL cylinder (Cylinder B), a mix 4.5 mL methanol with 1.5 mL DI water (Total volume =6mL) in another 10 mL cylinder (cylinder C), and a 0.25 mL 3-aminopropysiliane in syringe were measured respectively. Then the contents of cylinder A and cylinder C was mixed together in a 100mL beaker. Afterwards, the contents in cylinder B and in the syringe were added to the 100mL beaker and mixed together and the mixture was poured into 3mL cylindrical molds. Since the gelation occurs within 1 min, this step was performed as quickly as possible. The top surface of the mixture was kept wet with methanol during the curing in order to prevent cracking. Finally the molds were covered with parafilm to prevent contamination and allowed to stand for next 3 hrs. Sol-gels were removed from the molds carefully and without breakage. The sol-gels were placed in glass jars with closed lids containing methanol with approximately 4 times the volume of the monoliths and allowed to stand

for next 12-15 hrs at the room temperature and atmospheric conditions. The native monoliths were transferred from the methanol jars to glass jars containing acetronitrile (4 times the volume of aerogel monolith) and allowed to stand for next 12-15 hrs. The acetonitrile washing step was repeated three times. The next stage was carried out to crosslink the native sol-gel chain with isocyante solution. The crosslinker solution was prepared by mixing 33g of DESMADUR and 94 mL of acetonitrile in a 150 mL beaker. To crosslink the sol structure, the native monoliths were submerged into a newly prepared DESMADUR solution replacing the last utilized solvent and placed in an oven at 70 °C for 72 hrs. After 72 hrs of baking, the monoliths turned whitish in color but yet found to be translucent. Three more rounds of washes were carried out with acetonitrile after baking as well. Prepared monoliths were required to dry out by means of super critical drying process with liquid CO_2. This step was necessary to prevent the porous the skeleton of PCSA from collapsing due to the surface tension of the solvent. CO_2 was used as a drying medium because it is convenient, inexpensive, and environmentally acceptable. The drying process was carried out utilizing a critical point drier (CPD) acquired from Quorum technology, UK. The supercritical state of liquid CO_2 was reached at approximately 1300 psi and between 35-42^{0}C.

Bulk density of each synthesized PCSA cylinder was measured and averaged over each corresponding batch as described in Chapter 2. Each batch corresponds to a specific synthesized date and ten cylinders were synthesized for each batch. A sample standard deviation formula has been used to calculate the variation in densities among the samples which can occur during critical point drying. Figure 3.1 shows the calculated bulk density

distribution of PCSA over different batches. Synthesized PCSA monoliths after the CPD stage are shown in Figure 3.2.

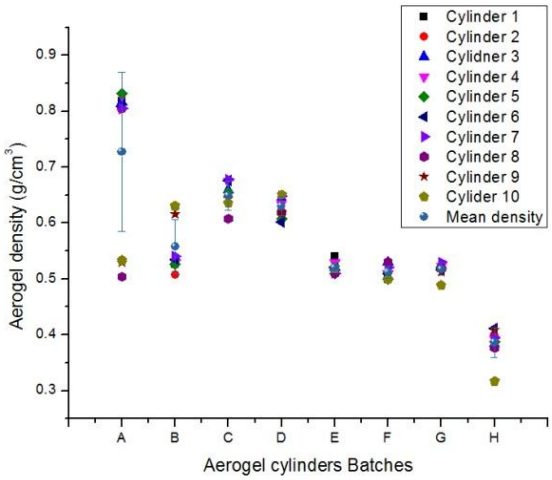

Figure 3.1: Bulk density distributions of PCSA for different batches.

Figure 3.2: Synthesized PCSA monoliths.

.

3.2 Pulverizing of polyurea crosslinked silica aerogel:

Initially a hand held nail homogenizer (Fisher Scientific Inc., PA) was utilized to pulverize PCSA cylinders. However, it became apparent that the PCSA was too hard for the grinder to perform consistently because the cutting edges wore away within a short period of time. In addition, the compartment was too small to fit a single cylinder. Therefore, a heavy duty stainless steel cutting blade-based pulverizer was acquired from IKA Works Inc., NC. PCSA cylindrical monoliths were pulverized with the help of a newly acquired grinder for 60sec. Notice that, the time constant of 60sec was set in accordance with the experimental outcome which is described later in this section. Then the PCSA particles were sorted out utilizing sieves (ASTM standard) having different mesh sizes: 20µm, 45µm, 90µm, 180µm, 300µm, and 425µm acquired from Fisher Scientific Inc. Finally PCSA particles have been found to be distributed over five different categories. Although we were able to obtain particles that fell into all the aforementioned categories but the distribution amount were not the same which was essential to prepare even number of samples from each category. Hence the following study was performed with only batch A.

Ten monoliths from batch A were ground five times in 30 sec intervals. The PCSA particles were sorted out each time and weighed. Initially, the distribution was dominated by larger PCSA particles but finally the distribution was found to be approximately even over the range of 425-90µm. It was concluded that the total pulverizing time of 60 sec could provide an approximately even distribution of PCSA particles in the aforementioned range. Three different PCSA size ranges obtained was:

425-300µm, 300-180µm, 180-90µm and the possible size ranges were: 425-300µm, 300-180µm, 180-90µm, 90-45µm, and 45-20µm.

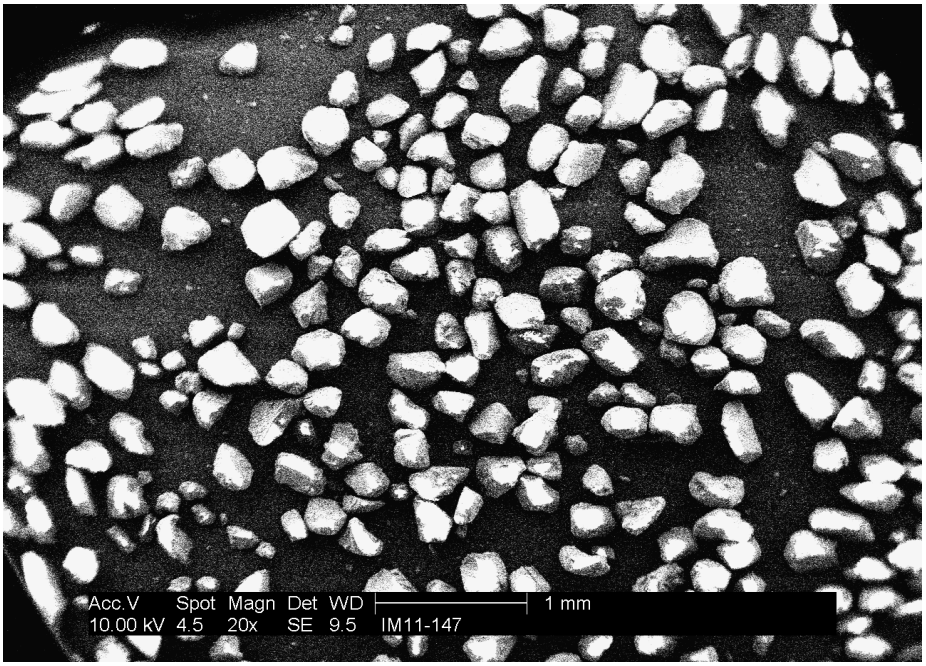

(a)

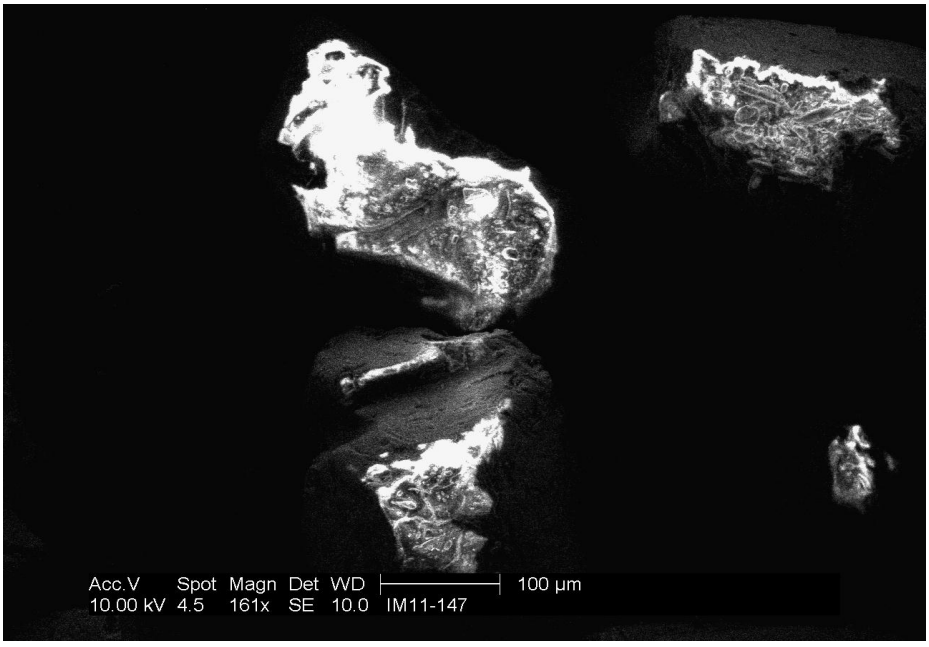

(b)

Figure 3.3: Scanning electron microscopy images of pulverized PCSA particles: (a) 1mm scale, and (b) 100µm scale.

3.3 PCSA-RTV 655 compound samples preparation:

ASTM standard (D1708-061) dog bone shaped Teflon molds, which were custom made in the College of Engineering machine shop, were utilized to cure neat RTV 655. However, the molds were found to be unreliable. As shown in Figure 3.4a, the molds deformed after several curing where performed at 100^0C . Therefore, a new set of aluminum molds of the same standards were acquired (Figure 3.4b) and polished by a professional mold polishing company (The Mold Polishing Inc., NJ). The type of polishing was SPI A-2.

(a) (b)

Figure 3.4: Sample preparation molds: (a) deformation of Teflon molds (right), (b) SPI-A2 polished aluminum mold.

RTV-655 and RTV-PCSA samples were cured in the polished aluminum molds in accordance with the ASTM standard D1708-06a (Fig.3.5). The polymer and crosslinker were mixed in a large container for 6 min at a mixing ratio of 10:1 as instructed by the manufacturers and the mixture was out gassed fully for 45 min in a vacuum chamber at a pressure of 20mbar. After the first round of out gassing stage, equal parts of neat polymer were poured into three different weigh boats and PCSA particles of three different size

ranges, 425-300μm, 300-180μm, and 180-90μm, were introduced into the polymer. For each particle size range, samples were made with a 25%, 50%, and 75% wt. of PCSA to RTV 655 as presented in Table 3. In all cases, the PCSA-RTV mixture was thoroughly and uniformly mixed prior to out gassing for a second time. After the second round of out gassing stage, the mixture was poured into the aluminum molds. The mixture was out gassed for the third time at a pressure of 15mbar and the mixture was cured at a temperature of 100^0C for 1 hr. The cured dog bone shaped samples were approximately 1.5 mm thick having the neck length of 22 mm and width of 5 mm (Figure 3.5).

Table 3 Fabricated Samples Category

Category	Combination	Embedded PCSA size (μm)	PCSA concentration to the RTV 655 wt.	Corresponding Volume percentage
1	RTV-655		0%	0%
	RTV-655 & PCSA	425-300	25%	42%
			50%	69%
			75%	87%
2	RTV-655		0%	0%
	RTV-655 & PCSA	300-180	25%	42%
			50%	69%
			75%	87%
3	RTV-655		0%	0%
	RTV-655 & PCSA	180-90	25%	42%
			50%	69%
			75%	87%

Figure 3.5: Prepared samples for tensile test.

3.4 Synthesis of amine functionalized polyoligomeric silsesquioxane crosslinked polyimide aerogels:

Preparation of n-oligomer POSS cross-linked PI aerogel monoliths is given below. 3,3,4,4-biphenyl tetreacarboxylic dianhydride (BPDA) and 4,4-methylenedianiline (MDA) was cross-linked with octa(aminophenyl) silsesquioxane (OAPS) in a solution of N-methyl-2-pyrrolidinone (NMP) and acetone respectively, to prepare polymide aerogel. Note that, BPDA and MDA is mixed at a ratio of (n+1) to n, where n is the number of repeat units of oligomers. The typical procedure for three monoliths is as follows: A 0.207g mass of MDA (2.09mmol), a 0.319g mass of BPDA (2.17mmol), and a 0.012g mass of OAPS (0.042mmol) were measured very carefully

with high precision scale acquired from OHAUS and separated in three different weigh boats labeled as A, B, and C, respectively. Volumes of 4.75 mL and 1.575 mL of NMP were measured with an adjustable volume pipette and placed in beaker A and beaker B respectively. The contents in weigh boat A were added in beaker A and stirred until it dissolved. The contents in weigh boat B were introduced to the solution in beaker A and stirred until it dissolved. The contents in weigh boat C were added to beaker B and stirred until it dissolved. The mixture was poured into beaker A and stirred for 10 minutes. A 1.640 mL of acetic anhydride (17.35mmol) and a 1.405 mL of pyridine (17.35mmol) were measured respectively in a pipette and added into beaker A successively and the solution stirred for another 10 min. The solution was poured into a Petri dish and allowed to stand for next 24 hrs. The gel was removed from the mold and soaked in NMP for 24hrs in a closed lead jar. The second round of wash was carried out by replacing old NMP solvent with a new mix of NMP & acetone (75% NMP & 25% acetone) for 24hrs. During third round of wash, the old NMP-acetone mixture was replaced by new mixture (25% NMP & 75% acetone) for 24hrs. Finally, the old solvent was replaced by 100% acetone and allowed to stand for another 24hrs. Prepared monoliths were required to be dry by means of super critical drying process as described in section 3.3.

3.5 RTV-PI compound samples preparation:

Amine functionalized POSS cross-linked polyimide aerogel was also utilized in the form of a dog bone in order to carry out the mechanical tests. An ASTM standard (D1708) cutting die (Pioneer DietechInc., MA) was utilized to punch the testing specimen from a thin sheet of POSS crosslinked PI. The cutting die was mounted in a manual toggle press in order to apply an even pressure distribution throughout the sheet.

Prepared samples have been utilized to perform mechanical tests at both room temperature (293K) and low temperature (77K). Figure 3.6 shows neat PI and RTV-PI compound samples utilized to perform the mechanical tests. Moreover neat PI in the form of strips were impregnated into RTV 655 to prepare RTV-PI compound samples of three differing area fractions (17%, 34%, and 51% PI cross sectional area to the neat polymer) by means of similar procedures as described in section 3.4.

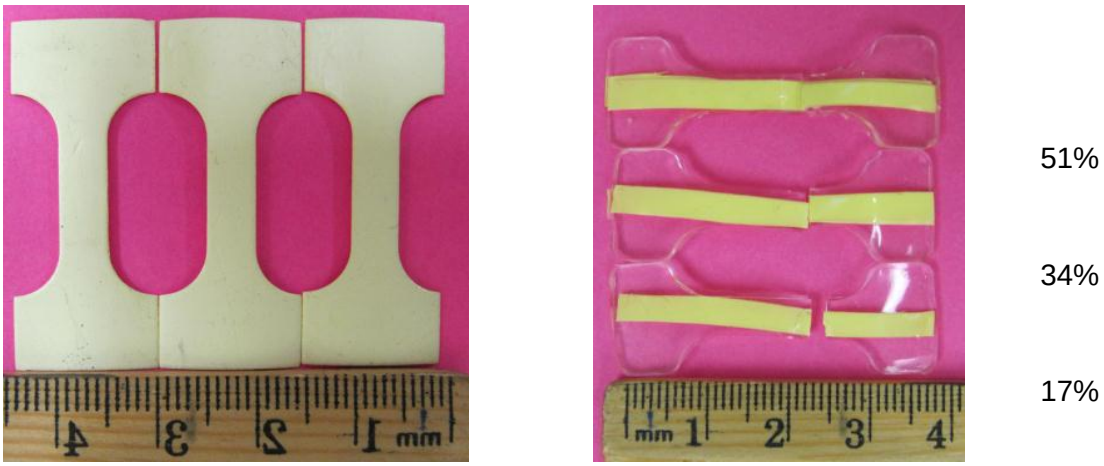

Figure 3.6: (a) Neat PI samples and (b) RTV-PI compound samples (post tensile testing).

Table 4 Fabricated PI/RTV samples category

Category	Combination	PI to the RTV 655 cross-sectional area fraction	Corresponding volume fraction
1	PI	0%	0%
	RTV-655 & PI	17%	22%
		34%	39%
		51%	56%

Chapter 4

EXPERIMENTAL SETUP

4.1 Tensile tester system:

A Mark-10 bench top motorized tensile tester: ESM 301 was used to perform all the mechanical tests. Force gauges used for this study alternated between BG 20 (capacity x resolution: 20 x 0.01lb) and BG 200 (capacity x resolution: 200 x 0.05lb) depending on the resolution and load requirement. The MESUR data acquisition software was used for all data acquisition and manipulations. Swivel adaptors were used for accurate alignment of specimen during testing. The clamps and the cryogenic container were custom designed and built in physics department instrument shop to fit the ESM 301 system. Initially commercially available grips including parallel jaw grips (G1013), and parallel paper and film grips (G1008) were used for testing but polymeric samples slipped during the extension period. Hence, a new set of clamps were custom designed and built in the machine shop (Figure 4.1) in order to address the slipping issue.

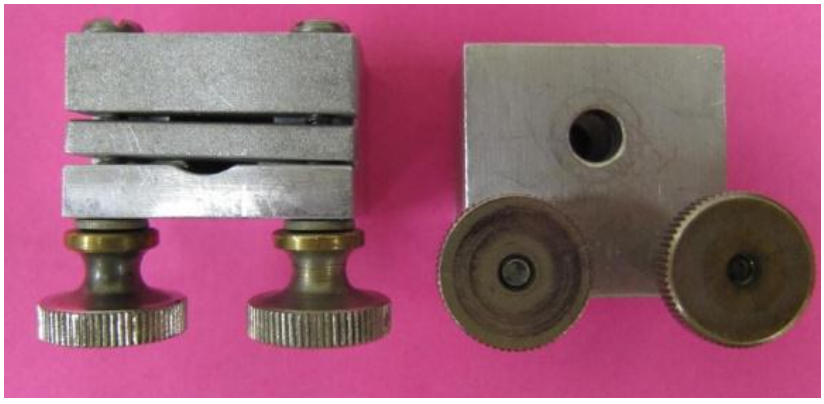

Figure 4.1: Custom made grips for the tensile tests.

4.2 Room Temperature Setup:

The room temperature test was conducted at approximately 293K (20^0C) under ambient conditions. A BG 200lbF force gauge was used to perform the tests. The test parameters were set up according to the ASTM standard for micro-tensile specimens as mentioned previously. A pull rate of 100mm/min was maintained for the duration of all tests.

(a) (b)

Figure 4.2: (a) Room temperature, and (b) low temperature experimental setup.

4.3 Low Temperature Setup:

The cryogenic container was made of aluminum and styrofoam. Liquid nitrogen was poured directly into the aluminum container and the styrofoam encased the aluminum container to provide insulation. The low temperature tests were performed at

77K (-196^{0}C) and in some cases at 197K (-76^{0}C). Once the sample had been mounted accurately within the custom-built grips and positioned on the stage, the sample plus the grips were lowered into the cryogenic container and liquid nitrogen/dry ice were dispensed into the cryostat. The container was filled up with liquid nitrogen/dry ice until the grips and the entire sample were immersed in cryogenic liquid. The lid of the container was then closed. The setup can be seen in Figure 4.2b. Testing parameters were the same as described in the room temperature test section.

Chapter 5

RESULTS AND DISCUSSIONS

In the first part (part A) of this chapter reports on the characterization of PCSA which includes bulk density measurements, optical characterizations, and gas adsorption report. Next the PCSA distribution after the pulverizing step is presented followed by the mechanical characterizations. In the second part of this chapter (Part B) the tensile results of POSS cross-linked PI and RTV-PI compound samples are reported and discussed.

Part A

Results of polyurea crosslinked silica aerogel-based impregnated RTV 655 measurements:

5.1 Optical characterization:

The UV-VIS absorbance and transmittance spectra of PCSA were obtained using a Beckman DU-60 UV-VIS spectrophotometer and are shown in Figure 5.1. PCSA are expected to be translucent in the visible range whereas in the case of Ultraviolet range they absorb heavily. Absorbance peaks are observed around 300-400nm (Figure 5a). On the other hand transmission (Figure 5b) through the specimen increases significantly as the wavelength of the incident beam increases towards the visible region.

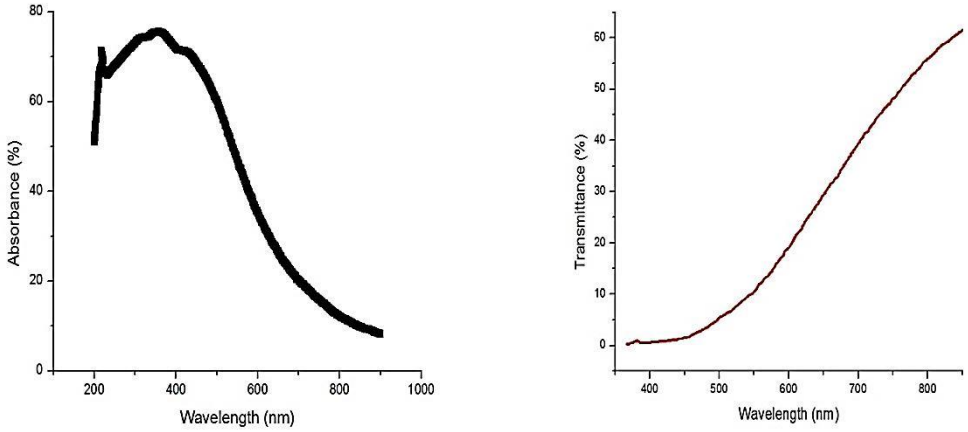

(a) (b)

Figure 5.1: (a) Absorbance and (b) transmittance spectra of PCSA monoliths.

5.2 Gas Adsorption Results:

A gas adsorption technique was carried out to characterize PCSA at nanometer and micrometer scale with help of a surface area and pore size analyzer machine: Autosorp 1 (Quantachrome Instruments, Beijing, China). The summary of results is provided in Table 5 in accordance with different models described in Chapter 2, section 2.4.

Table 5 Nitrogen gas adsorption results

Parameter	Analyzing method	Results
Surface area data, m^2/g	Multipoint BET	70.60
	Langmuir surface area	13.07
	BJH method	54.22
	DH method	56.92
	t-method external surface area	70.60
	DR method micro pore area	102.0
Pore volume, cc/g	Total pore volume for pores with diameter 26.2$\dot{A}$	0.0338
	BJH method cumulative pore volume	0.0281
	t-method pore volume	0.0283
	DR micro pore volume	0.0362
	HK cumulative pore volume	0.0251
	SF cumulative pore volume	0.0259
Pore size, $\dot{A}$	Average pore diameter	19.18
	BJH pore diameter	24.84
	DR micro pore diameter	15.69
	HK pore diameter	17.27
	SF pore diameter	32.76

5.3 Pulverizing results:

The effect of grinding time on PCSA particles size distribution is also investigated as mentioned in chapter 3 (Figure 5.2). The particle size ranges were d>425µm, 425-300µm, 300-180µm, 180-90µm, 90-45µm, and 45-20µm. A grinding time of 60sec provided with a consistent mass distribution of PCSA particles over the range of 425-90µm. It was found that approximately 60% of the PCSA particles fell into the following three ranges: 425-300µm, 300-180µm, and 180-90µm.

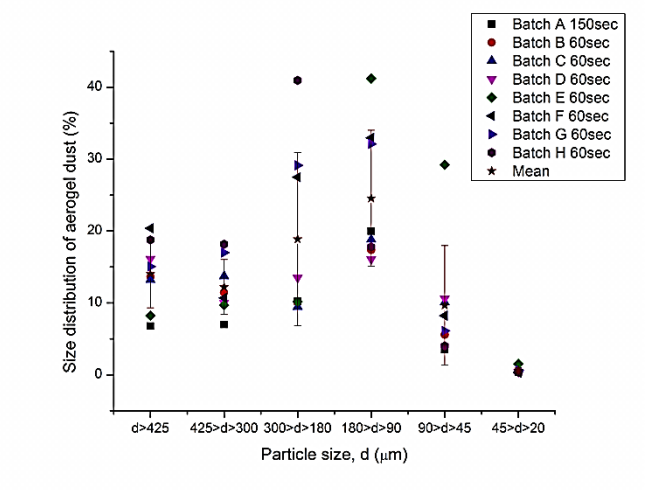

Figure 5.2: PCSA particle size distributions.

5.4 Mechanical characterizations:

Tensile tests were carried out on both neat polymer (RTV 655) and RTV-PCSA compound samples at two different temperatures of 293K and 77K. Overall, the mechanical picture of the compound material was also evaluated with the help of stress-strain profile as described in the Chapter 2.

Neat polymer behavior at room temperature (293K):

Figure 5.3 represents stress vs. strain plots of neat RTV 655 of nine separately synthesized samples from three different batches. The obtained tensile profile of the neat polymer followed the standard tensile profile of elastomeric polymers[52,53].

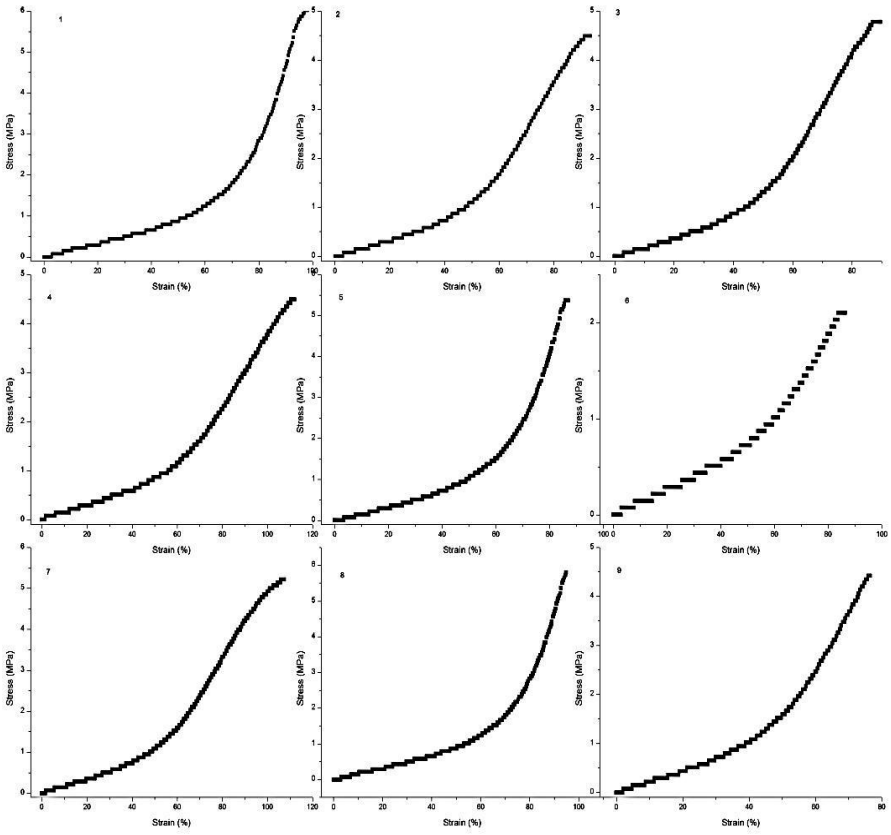

Figure 5.3: Tensile profile of neat polymer (RTV 655) obtained at 293K.

A summarized tensile report of the neat polymer is also presented in Table 6.

The uncertainty value that has been included to show the variation is calculated utilizing the sample standard deviation formula. It can be seen that the tensile behavior of neat polymer samples from all the batches was quite reproducible at 293K except for the fact that there was a small variation in the rupture strain and stress. Although great care was taken to be consistent during the sample preparation stage and testing protocol, batch to batch variations were inevitable to a small degree. Other factors that could have contributed to the variations in the tensile strength include the utilization of dog bone cavity molds instead of cutting die which will be discussed later. Nevertheless, the rupture stress of 4.65MPa on average compared to 6.5MPa of that reported by the manufacturer and the on average rupture strain of 99.44% compared to the elongation of 120% reported by the manufacturer exhibits a consistence performance.

Table 6 Rupture stress and strain at 293K

Sample number	Stress to failure, MPa	Mean, MPa	Strain to failure, %	Mean, %
1	6.0		100	
2	4.5		90	
3	5.0		85	
4	5.0	4.6±1.0	120	99±14
5	5.5		100	
6	2.2		100	
7	5.0		120	
8	5.5		100	
9	4.5		80	

Neat polymer behavior at 197K:

The low temperature behavior of neat polymer was assessed at 197K by performing mechanical tests in a dry ice bath. Investigation with dry ice revealed the elastomeric behavior of RTV 655 even at 197K and is shown in Figure 5.4. Three samples are tested from the same batch and cured under the same conditions.

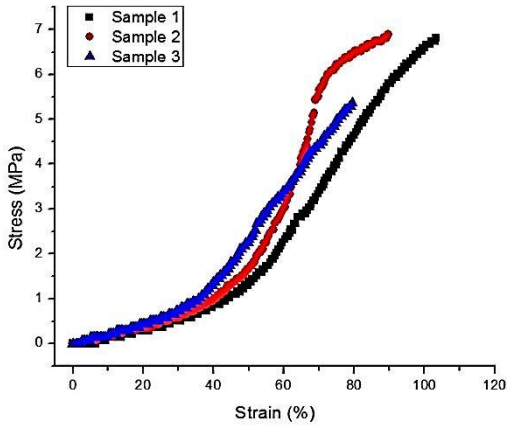

Figure 5.4: Tensile profile of RTV 655 at 197K.

Neat polymer behavior at77K:

Figure 5.5 represents the tensile profile of neat polymers from all batches at 77K. The tensile behavior of RTV 655 at 77K demonstrates a significant strengthening of the polymer perhaps due to the significant amount of stiffening in the polymer chain [47,59]. Normally the stiffness of the polymer chain results in rupture at a very low strain and a very high load[60]. Some variation in the rupture stress was noted, but the overall tensile profile of all the samples was found to be similar to each other. Rupture stress and rupture strain is summarized in Table 7 for convenience. The variation in results is likely

attributable to the factors already discussed earlier. Moreover, the actual temperature of the testing samples could vary slightly due to the heat exchange between the liquid nitrogen and testing samples. Nevertheless by taking into account all the aforementioned factors, the obtained results were consistent and demonstrated repeatability.

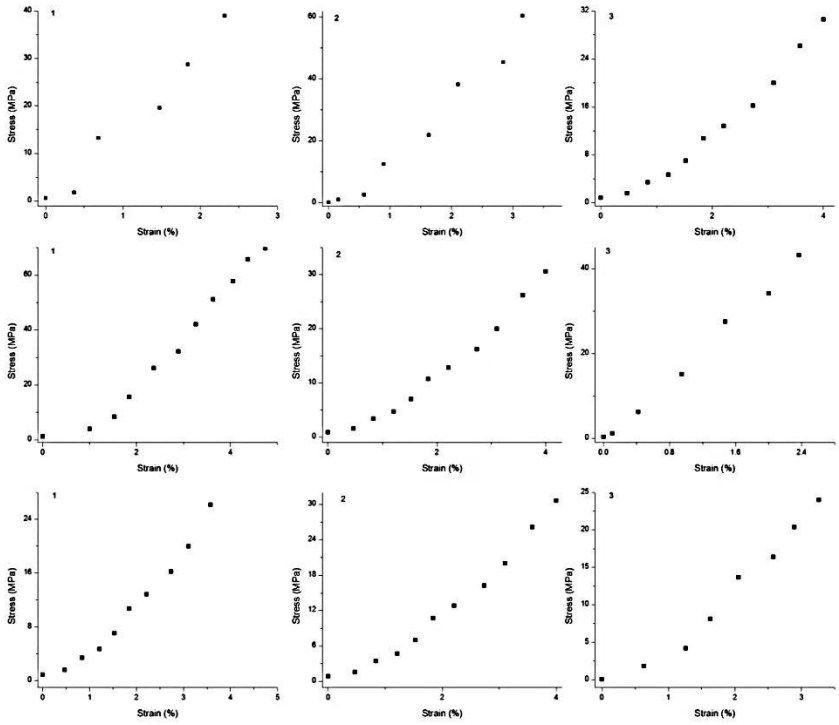

Figure 5.5: Tensile behavior of neat RTV 655 at 77K.

Table 7 Rupture stress and strain at 77K

Sample number	Stress to failure, MPa	Mean, MPa	Strain to failure, %	Mean, %
1	40		2.8	
2	60		3.4	
3	32		4.0	
4	62	40±14	4.5	3.7±0.64
5	35		4.0	
6	45		2.4	
7	27		4.0	
8	32		4.0	
9	25		3.4	

RTV-PCSA behavior at room temperature (293K):

Effect of PCSA concentration on mechanical properties of RTV-PCSA:

The tensile behavior of PCSA-RTV compound material is demonstrated in Figure 5.6 as a function of PCSA concentration levels. A general trend towards the more brittle profile was observed (considering 25 wt. % specimen brittle itself which we will be discussed later) as the incorporation level increases regardless of PCSA particle sizes (Figure 5.6). Figure 5.6a illustrates the tensile behavior of the RTV-PCSA compound samples incorporated with the largest PCSA particle size (425-300μm). It is obvious that at an impregnation level of 25 wt. % the compound specimen ruptures at a relatively higher strain (approximately 45%) compared to the 50 wt. % and 75 wt. % compound samples of that which is less than 5% (Figure 5.6a-c). As described in Chapter 2, the nature of a brittle material is to rupture at a very low elongation which was the observed here as well. Several plateaus were observed in the tensile profile for the 25 wt. % impregnated samples regardless of PCSA sizes marked as A and B (Figure 5.6c). This

strange behavior could be explained as follows. These plateaus indicate the phenomenon of rapid crack propagation which could be an effect of aggregation of the PCSA particles at a specific place into the RTV matrix. It could be the result of the inhomogeneous dispersion of the PCSA into the polymer matrix. Notice that the mechanical properties of any filler matrix also depends on the dispersion of the filler over the entire matrix[54]. A simple mathematical treatment reveals that an aggregation of approximately 30 PCSA particles next to each other could lead to crack propagation from point A to B. The mathematical treatment was carried out assuming perfectly spherical PCSA particles with the diameter of 135μm; the average of the range 180-90μm. Those plateaus mentioned are not observed in the case of 50 wt. % and 75 wt. % simply because the specimens ruptured at the very moment of pulling during the test and can be verified from the fact that the strain to rupture was less than 5% which is about 2mm in length.

The comparison of the tensile profile of the compound samples with the neat polymer is shown in Figure 21d. The inset represents a zoomed in section of the plot. The comparison reveals the fact that the breakage of the 50 wt. % and 75 wt. % impregnated specimens occurred at such a low strain where the necking of neat polymer has not been even initiated. However the 25 wt. % impregnated samples stretched out much further to exhibit relatively higher toughness as compared to other compound samples. The tensile strength of this particular category was yet found to be very low compared to neat polymer of that. It is apparent that PCSA-RTV composites exhibit a non-linear relationship between stress and strain which made it very difficult to calculate the Young's modulus from the tensile profile. But even if an attempts were made to calculate Young's modulus by taking into account the very initial portion of the curves

which could essentially be only two date points then the slopes would appear as shown in the inset of Figure 5.6d. Certainly Figure 5.6d reveals the fact of increasing Young's modulus as an increasing function of PCSA loading into polymer matrix.

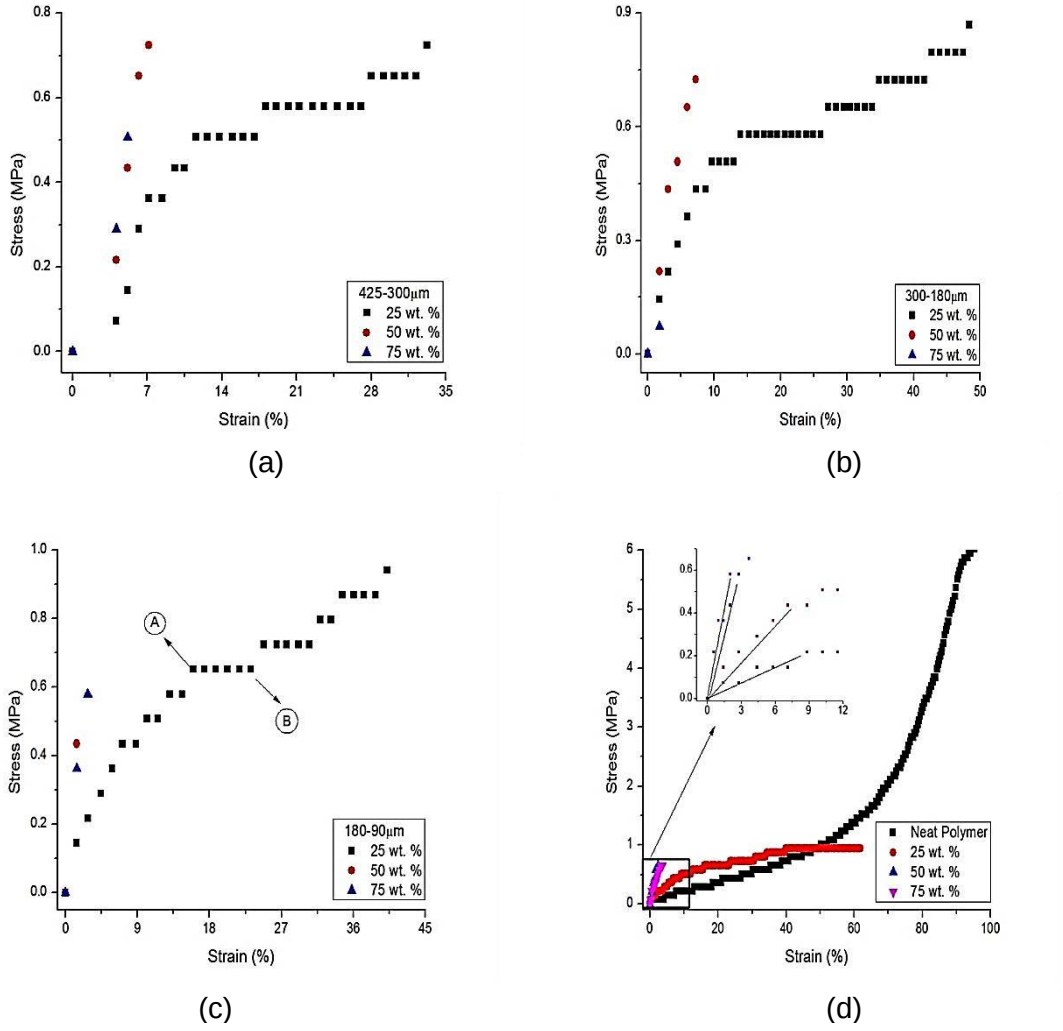

Figure 5.6: Effect of PCSA concentration on mechanical properties. Tensile profile set for three different PCSA sizes (a) 425-300µm, (b) 300-180µm, and (c) 180-90µm, and (d) comparison of tensile behavior with neat polymer at 293K.

Effect of PCSA particle size on mechanical properties of RTV-PCSA:

The effect of particle size on the mechanical properties has been reported in several studies[25,57,58]. A slight increase in the Young's modulus has been reported for the higher volume fraction (15%) with reduction of embedded particle sizes (from 35nm to 15nm) whereas the modulus was found to be independent of the particle sizes for lower volume fraction (5%)[58]. For that particular study[58], however, the embedded silica/glass particles were spherical in shape ranging from 3nm to 30μm. In contrast, The range of PCSA incorporated in this study varied from 90μm to 425μm.. Moreover, the SEM images (Figure 2.12) revealed that the geometry of the PCSA particles were non-uniform in shapes and many particles had sharply pointed edges. The tensile profile of RTV-PCSA compound materials was found to be independent of PCSA particle size (Figure 5.7). It was also observed that the strain to failure was independent of PCSA size at a specific impregnation level. Moreover, a similar approach is also taken here to illustrate the dependency of Young's modulus on the PCSA size as described in the previous section. From the presented slopes in the inset of Figure 5.7d, it can be seen that the Young's modulus was found to be independent of PCSA particle size. The factors that interplayed here were: relatively very large PCSA sizes, wide distribution of PCSA sizes (425-90μm), and random shapes of PCSA especially those with sharp edges.

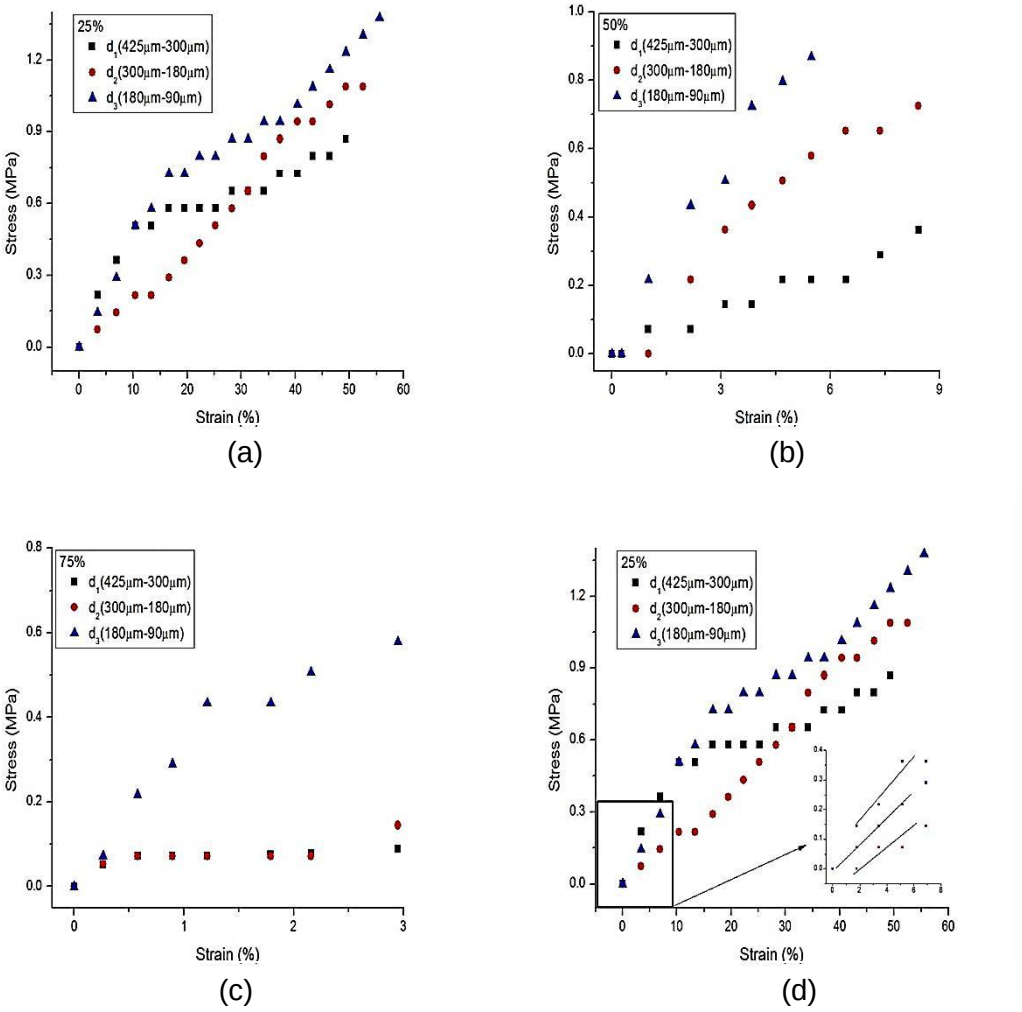

Figure 5.7: Effect of PCSA size on mechanical properties. Representative stress vs. strain curves for the samples impregnated at (a) 25 wt. %, (b) 50 wt. %, and (c) 75 wt. %, and (d) comparison of tensile behavior with neat polymer at 293K.

Summary of RTV-PCSA at 293K:

Tensile strengths (i.e. stress to failure or rupture) are reported both as a function of PCSA concentrations and sizes in Figure 5.8a-c. A drastic reduction in the tensile strength was observed due to incorporation of PCSA compared to the neat polymer of that (Figure 5.8a-b). The reduction in strength was substantial for the case of highly impregnated compound samples (50 wt. % and 75 wt. %). However, a comparatively small amount of reduction in the tensile strength was observed for the case of 25 wt. % impregnation samples incorporated with the smallest PCSA particles: 180-90μm (Figure 5.8c). Nonetheless, at higher concentration levels (50 wt. % and 75 wt. %) the tensile strength was found to be independent of PCSA sizes (Figure 5.8c). The variation in the modulus of toughness is reported in Figure 5.8d. The modulus of toughness is a commonly used parameter in the field of fracture mechanics. The modulus of toughness was calculated by integrating the area under the stress vs. strain curve of a sample. A drastic reduction in the modulus of toughness was observed due to the incorporation of PCSA into the polymer matrix and was found to be independent of PCSA sizes. However the modulus of toughness calculated for the lowest impregnated samples (25 wt. %) was found to be relatively higher when compared to the highly impregnated sample (50 wt. % and 75wt. %).

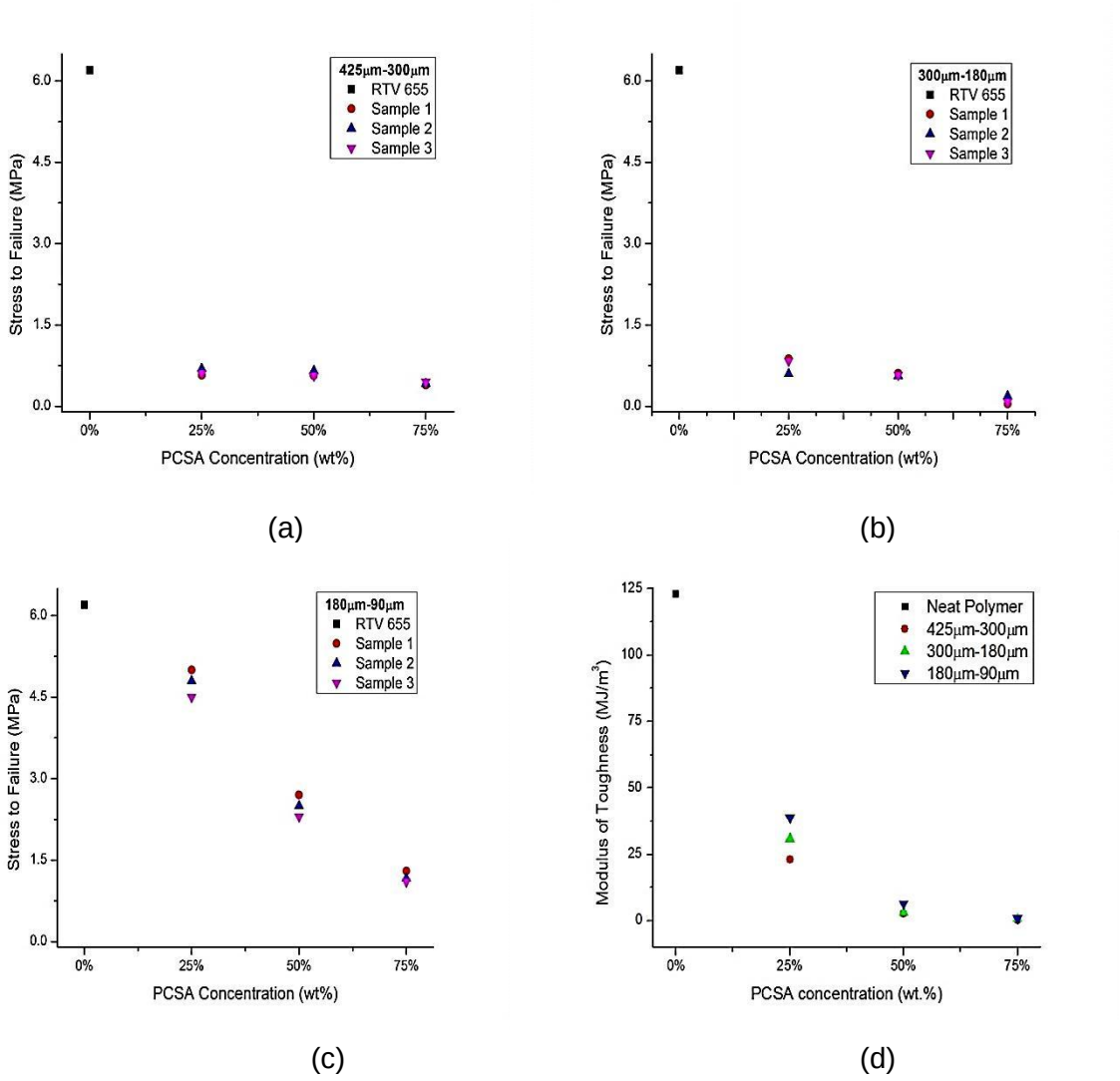

Figure 5.8: Comparison of tensile strength (a) 425-300µm, (b) 300-180µm, and (c) 180-90µm impregnated samples, and (d) comparison of average modulus of toughness as a function of PCSA size and concentration at 293K.

RTV-PCSA behavior at liquid nitrogen bath (77K):

Effect of PCSA concentration:

The effect of PCSA concentration on the tensile profile at 77K is shown in Figure 5.9. In contrast to the room temperature results, the tensile profile of the compound material was observed to be independent of PCSA concentration at low temperature. However, a significant amount of increase in the tensile strength was observed at 77K compared to the 293K results of that. At the cryogenic temperature of 77K, the RTV-PCSA compound samples were found to be relatively stiffer and more brittle when compared to the behavior of samples investigated at 293K (Figure 5.6 and 5.9). Although the tensile profile was found to be independent of PCSA impregnation level, an enhancement in the tensile strength was observed as a decreasing function of PCSA size at a specific impregnation level (Figure 5.9a-c). The comparison of the tensile profiles between the compound materials and the neat polymer is also shown (Figure 5.9d). The tensile profile of neat polymer and compound matrix was found to be similar at 77K. A similar approach as mentioned earlier was carried out to picture the Young's modulus under this condition as well (Figure 5.9d: inset). It is obvious from the inset diagram that the Young's modulus was found to be independent of PCSA concentrations at 77K.

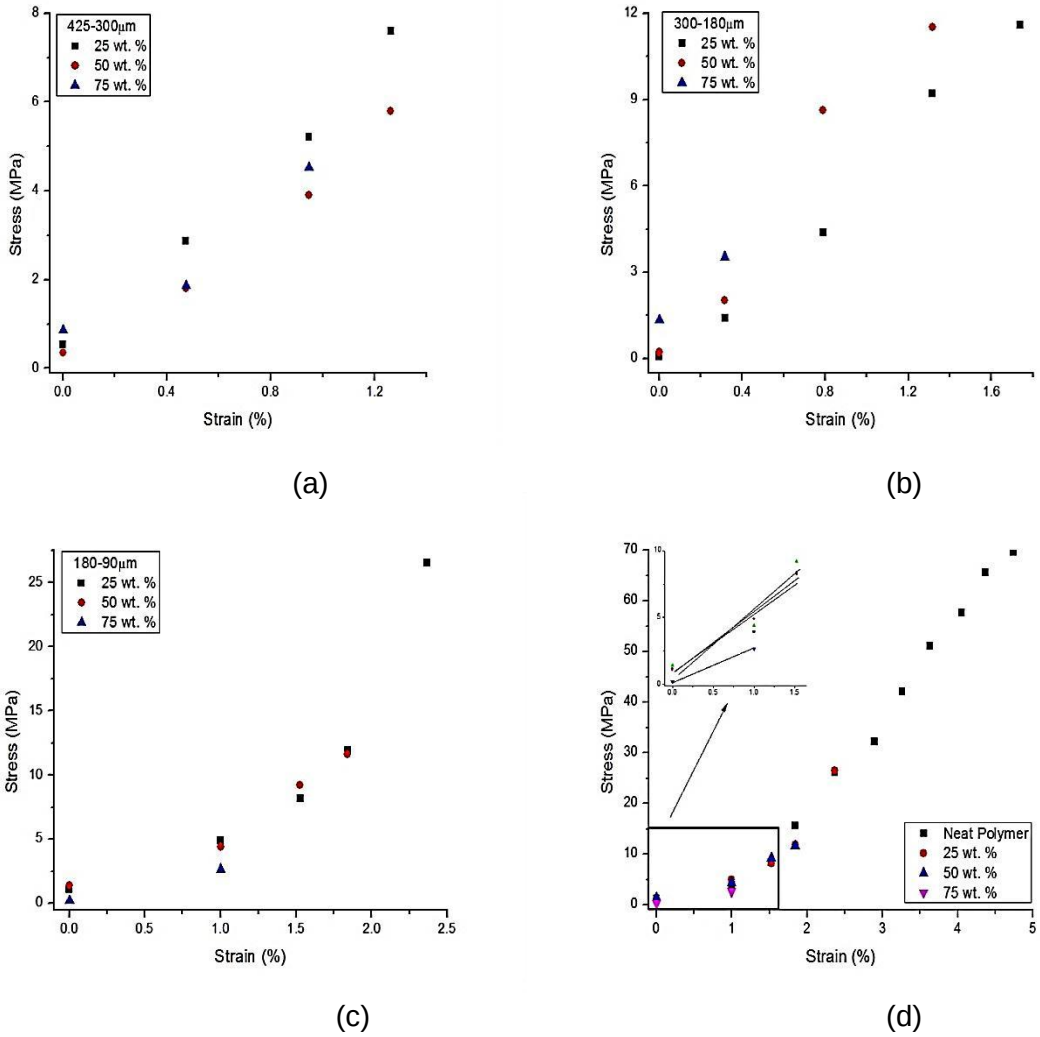

Figure 5.9: Effect of PCSA concentrations on the mechanical properties. Tensile profile set for three different PCSA sizes (a) 425-300µm, (b) 300-180µm, and (c) 180-90µm, and (d) comparison of tensile behavior with neat polymer at 77K.

Effect of PCSA particle sizes on mechanical properties:

The tensile profile of RTV-PCSA compound samples as a function of PCSA sizes at 77K is shown in Figure 5.10. At 77K, the tensile profile of the proposed compound material was found to be independent of PCSA size similar to the behavior that was observed at room temperature. Again, a similar approach has been carried out to illustrate the independence of Young's modulus on PCSA size (Figure 5.10d: inset).

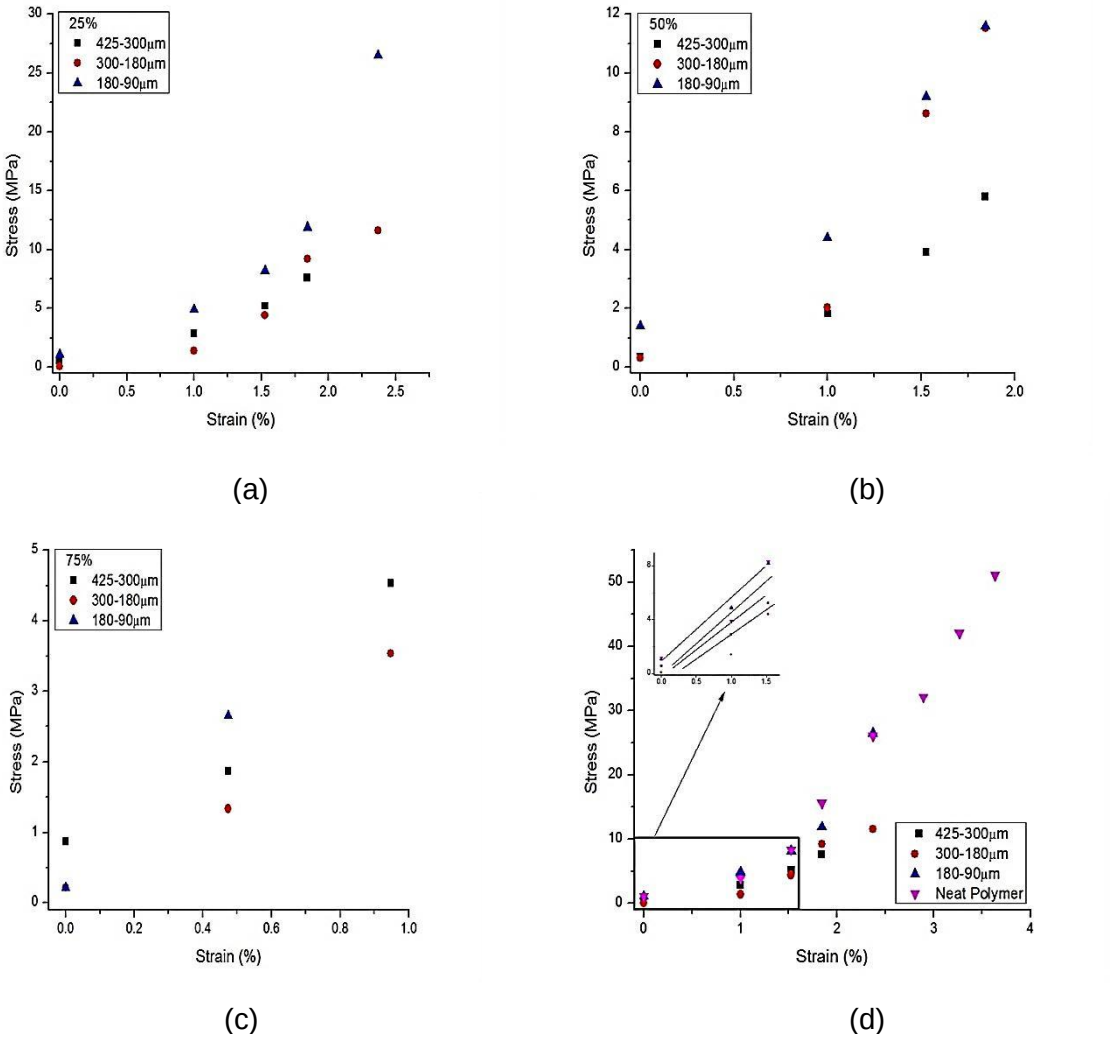

Figure 5.10: Effect of PCSA size on mechanical properties. Representative stress vs. strain curves for the samples impregnated at (a) 25 wt. %, (b) 50 wt. %, and (c) 75 wt. %, and (d) comparison of tensile behavior with neat polymer at 77K.

Summary of results for RTV-PCSA at 77K:

In summary, the tensile strength of RTV 655 matrix was reduced due to the incorporation of PCSA. The trend of decreasing rupture strength at 77K (Figure 5.11) was similar to the trend observed at 293K (Figure 5.6) as a function of PCSA concentration. However, the compound sample impregnated at a 25 wt. % with the finest PCSA (180-90μm) exhibited comparatively stronger behavior when compared to the compound samples from other categories (Figure 5.11 a-c). Finally, the modulus of toughness has been calculated similarly as described earlier and found to be significantly reduced. As shown in Figure 5.11d, the modulus of toughness is also independent of PCSA impregnation level and particle size.

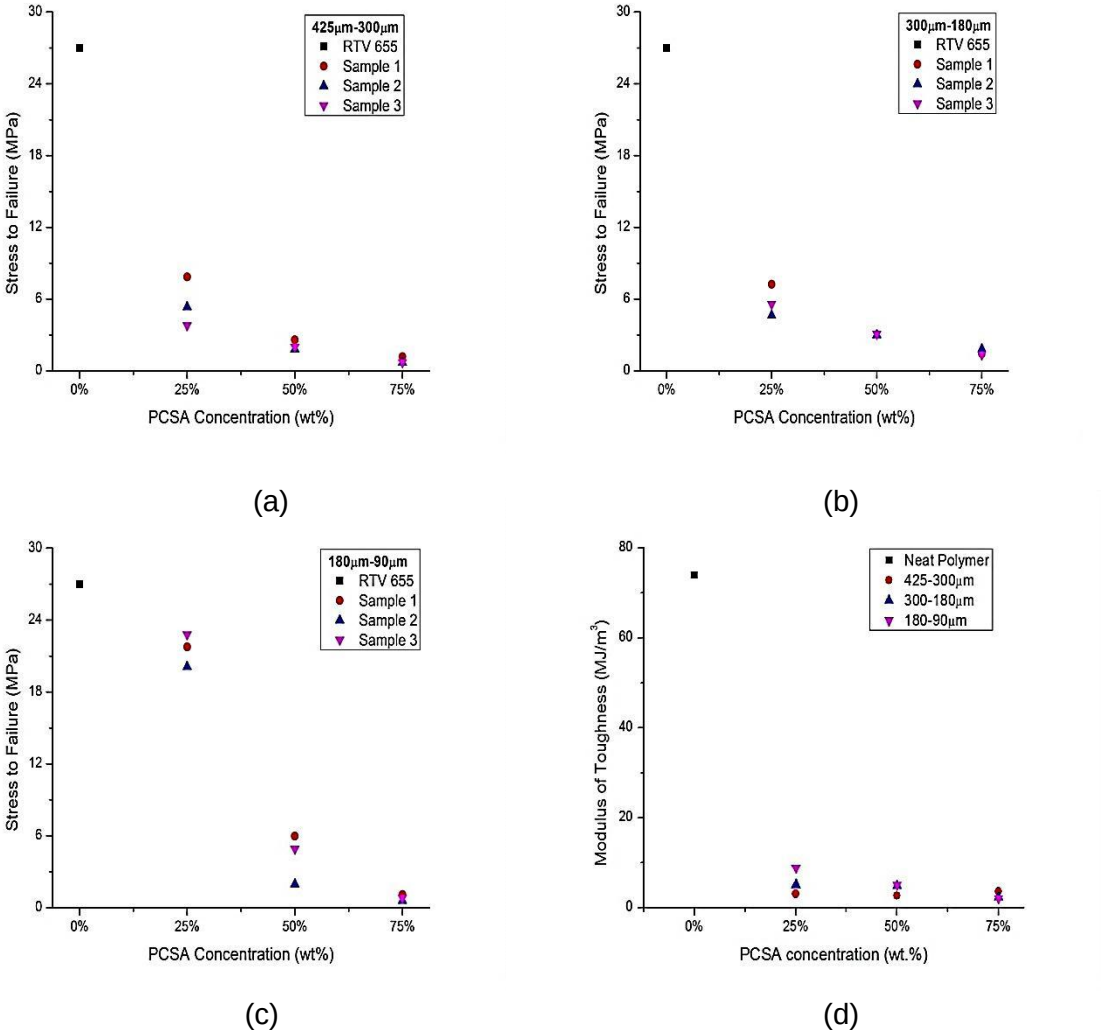

Figure 5.11: Comparison of tensile strength (a) 425-300µm, (b) 300-180µm, and (c) 180-90µm impregnated samples, and (d) comparison of average modulus of toughness as a function of PCSAsize and concentration at 77K.

Part B

Results of polyimide based impregnated RTV 655 measurements:

This part of the Chapter contains the tensile results of neat amine functionalized POSS crosslinked polyimide aerogel at both 293K and 77K as well the tensile properties of RTV-PI compound samples at 293K.

Neat Polyimide (PI) behavior at room temperature:

The tensile profile of neat PI samples at 293K is shown in Figure 5.12 which in fact demonstrates the brittle nature of PI. The specimens ruptured at a low strain percentage. The summary of the results presented in Table 8 illustrate a significant level of repeatability in these particular tests. . The reproducibility is likely due to the utilization of cutting die to prepare the samples instead of cavity molds.

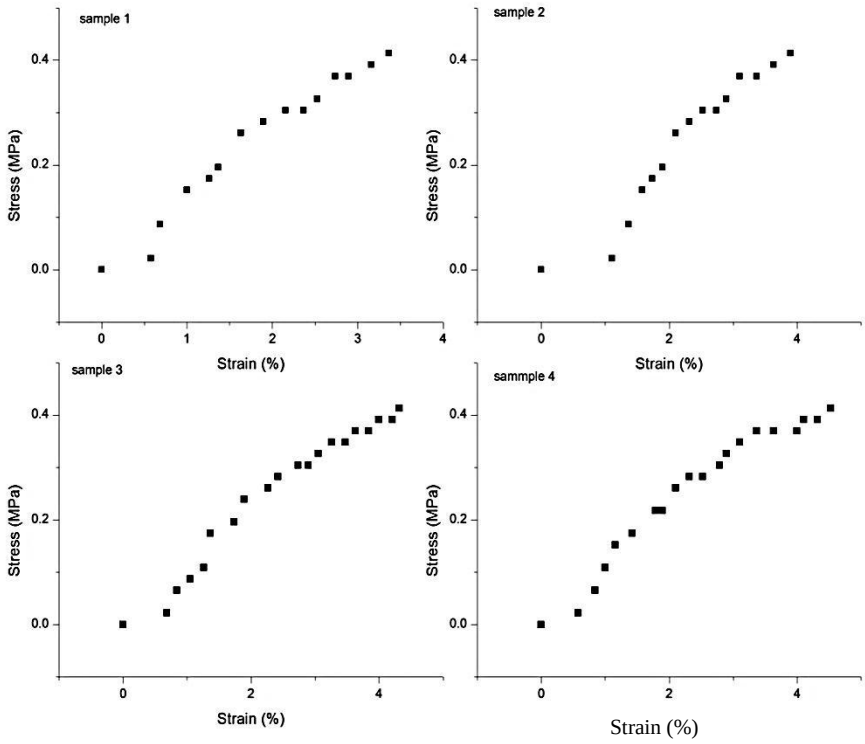

Figure 5.12: Neat PI tensile profile at 293K.

Table 8 Rupture stress and strain of PI at 293K

Sample number	Stress to failure, MPa	Mean, MPa	Strain to failure, %	Mean, %
1	4.1		3.6	
2	4.1	4.1±0.0	4.6	4.2±0.4
3	4.1		4.5	
4	4.1		4.1	

Stress-strain behavior of PI aerogels at 77K:

The tensile profile of neat PI at 77K is shown in Figure 5.13. The tensile behavior of neat PI was found to be similar at both 77K and 293K. Neat PI was found to be brittle at both the temperatures as the samples ruptured at similar strain percentages. Again, the obtained results were consistent for the four tested samples which affirm the repeatability of the experiment (Table 9).

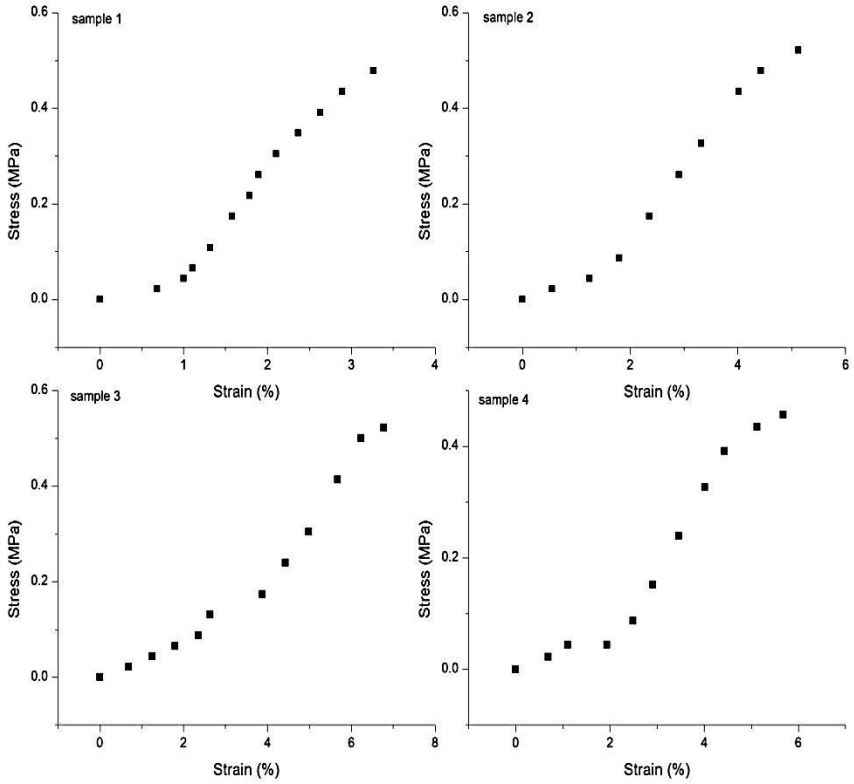

Figure 5.13: Neat PI tensile profile at 77K.

Table 9 Rupture stress and strain of PI at 77K

Sample number	Stress to failure, MPa	Mean, MPa	Strain to failure, %	Mean, %
1	4.7		3.2	
2	5.2	4.7±0.6	5.1	4.9±1.4
3	5.2		6.7	
4	3.9		4.7	

Polyimide impregnated RTV 655 behavior at room temperature:

A preliminary study has been carried out on RTV-PI compound samples at a varying cross sectional area fractions of 17%, 34%, and 51% to the polymer at 293K. The tensile profile obtained from this investigation is shown in Figure 5.14a as a function of area fractions. The rupture load as a function of area fraction is shown in Figure 5.14b. A reduction in the tensile strength was observed as an increasing function of area fractions.

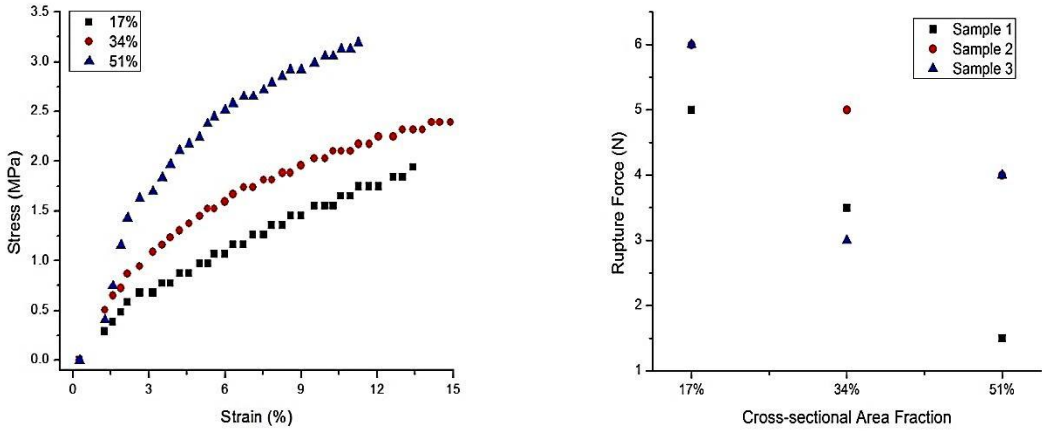

(a) (b)

Figure 5.14: (a) Tensile profile and (b) rupture load of RTV-PI compound sample.

The RTV-PI compound samples exhibit similar trend in the reduction of tensile strength as a function of increasing volume fractions as the RTV-PCSA compound samples at 293K. However, the 25 weight (wt.) % impregnated RTV-PCSA compound samples with the smallest PCSA particles (180-90μm) were found to rupture at greater strain percentage compared to the lowest impregnated RTV-PI compound samples.

Chapter 6

CONCLUSION

The effect on the tensile properties due the introduction of PCSA particles into a polymer matrix has been investigated for a prospect of future cryogenic tank applications. The effect of PCSA size and concentration on the uniaxial tensile behavior has been reported at both 293K and 77K. The mechanical properties of the compound material were found to be independent of PCSA particle size for the range of sizes studied at both 293K and 77K for the higher concentration values. The tensile behavior of the compound material seemed to have a stronger dependency on the PCSA concentrations at both reported temperatures. Some irregularity was observed in the stress vs. strain curves obtained from the compound materials and this is attributed to a number of parameters but predominantly to the relatively large PCSA sizes variations in each group, geometrical non uniformities of each particle, and variations in the particle size distribution from batch to batch.

On the other hand, neat PI was found to produce highly reproducible and consistent stress vs. strain curves as well as relatively similar mechanical strength at both 293K and 77K. RTV-PI and RTV-PCSA room temperature results were found to be comparable.

Future study

It is recommended for the future study to identify mechanisms that can create small spherical PCSA particle sizes since it is expected that the incorporation with spherically shaped smallest PCSA would be more reproducible and closer to the non-impregnated behavior of the RTV 655 both at room temperature and at low temperatures.

Moreover spherically shaped PCSA particles could increase the mechanical strength of the compound materials by several orders of magnitude. Also, the RTV-PI investigation should be carried out at low temperature to compare the strength of that with RTV-PCSA materials at the same condition.

References

1 *Aerogels handbook*. (Springer, 2011).

2 Yoldas, B. E., Annen, M. J. & Bostaph, J. Chemical Engineering of Aerogel Morphology Formed under Nonsupercritical Conditions for Thermal Insulation. *Chemistry of Materials*12, 2475-2484, doi:10.1021/cm9903428 (2000).

3 Novak, K. S., Phillips, C. J., Birur, G. C., Sunada, E. T. & Pauken, M. T. Development of a Thermal Control Architecture for the Mars Exploration Rovers. *AIP Conference Proceedings*654, 194-205 (2003).

4 Tsou, P. Silica aerogel captures cosmic dust intact. *Journal of Non-Crystalline Solids*186, 415-427, doi:10.1016/0022-3093(95)00065-8 (1995).

5 Carlson, P. Aerogel Cherenkov counters: Construction principles and applications. *Nuclear Instruments and Methods in Physics Research Section A: Accelerators, Spectrometers, Detectors and Associated Equipment*248, 110-117, doi:10.1016/0168-9002(86)90503-6 (1986).

6 Reynolds, J. G., Coronado, P. R. & Hrubesh, L. W. Hydrophobic aerogels for oil-spill clean up – synthesis and characterization. *Journal of Non-Crystalline Solids*292, 127-137, doi:10.1016/s0022-3093(01)00882-1 (2001).

7 Katti, A. *et al.* Chemical, Physical, and Mechanical Characterization of Isocyanate Cross-linked Amine-Modified Silica Aerogels. *Chemistry of Materials*18, 285-296, doi:10.1021/cm0513841 (2005).

8 Meador, M. A. B. *et al.* Reinforcing polymer cross-linked aerogels with carbon nanofibers. *Journal of Materials Chemistry*18, 1843-1852 (2008).

9 Meador, M. A. B., Capadona, L. A., McCorkle, L., Papadopoulos, D. S. & Leventis, N. Structure−Property Relationships in Porous 3D Nanostructures as a Function of Preparation Conditions: Isocyanate Cross-Linked Silica Aerogels. *Chemistry of Materials*19, 2247-2260, doi:10.1021/cm070102p (2007).

10 Luo, H. *et al.* Synthesis and characterization of the physical, chemical and mechanical properties of isocyanate-crosslinked vanadia aerogels. *Journal of Sol-Gel Science and Technology*48, 113-134, doi:10.1007/s10971-008-1788-y (2008).

11 Hsueh, C.-H. Effects of Aspect Ratios of Ellipsoidal Inclusions on Elastic Stress Transfer of Ceramic Composites. *Journal of the American Ceramic Society*72, 344-347, doi:10.1111/j.1151-2916.1989.tb06132.x (1989).

12 Pukánszky, B. Interfacial interactions in particulate filled thermoplastics: Mechanism, strength, properties. *Makromolekulare Chemie. Macromolecular Symposia*70-71, 213-223, doi:10.1002/masy.19930700123 (1993).

13 Nakamura, Y., Yamaguchi, M., Okubo, M. & Matsumoto, T. Effects of particle size on mechanical and impact properties of epoxy resin filled with spherical silica. *Journal of Applied Polymer Science*45, 1281-1289, doi:10.1002/app.1992.070450716 (1992).

14 Reynaud, E., Jouen, T., Gauthier, C., Vigier, G. & Varlet, J. Nanofillers in polymeric matrix: a study on silica reinforced PA6. *Polymer*42, 8759-8768, doi:10.1016/s0032-3861(01)00446-3 (2001).

15 Ou, Y., Yang, F. & Yu, Z.-Z. A new conception on the toughness of nylon 6/silica nanocomposite prepared via in situ polymerization. *Journal of Polymer Science Part B: Polymer Physics*36, 789-795, doi:10.1002/(sici)1099-0488(19980415)36:5<789::aid-polb6>3.0.co;2-g (1998).

16 Zhu, Z.-K., Yang, Y., Yin, J. & Qi, Z.-N. Preparation and properties of organosoluble polyimide/silica hybrid materials by sol–gel process. *Journal of Applied Polymer Science*73, 2977-2984, doi:10.1002/(sici)1097-4628(19990929)73:14<2977::aid-app22>3.0.co;2-j (1999).

17 Dekkers, M. E. J. & Heikens, D. The effect of interfacial adhesion on the tensile behavior of polystyrene–glass-bead composites. *Journal of Applied Polymer Science*28, 3809-3815, doi:10.1002/app.1983.070281220 (1983).

18 Fu, S.-Y. & Lauke, B. Characterization of tensile behaviour of hybrid short glass fibre/calcite particle/ABS composites. *Composites Part A: Applied Science and Manufacturing*29, 575-583, doi:10.1016/s1359-835x(97)00117-6 (1998).

19 Fu, S.-Y. & Lauke, B. Fracture resistance of unfilled and calcite-particle-filled ABS composites reinforced by short glass fibers (SGF) under impact load. *Composites Part A: Applied Science and Manufacturing*29, 631-641, doi:10.1016/s1359-835x(97)00111-5 (1998).

20 Liang, J. Z., Li, R. K. Y. & Tjong, S. C. Morphology and tensile properties of glass bead filled low density polyethylene composites: MATERIAL PROPERTIES. *Polymer Testing*16, 529-548, doi:10.1016/s0142-9418(97)00017-2 (1998).

21 Varlet, J., Cavaillé, J. Y., Perez, J. & Johari, G. P. Dynamic mechanical spectrometry of nylon-12. *Journal of Polymer Science Part B: Polymer Physics*28, 2691-2705, doi:10.1002/polb.1990.090281315 (1990).

22 Danusso, F. & Tieghi, G. Strength versus composition of rigid matrix particulate composites. *Polymer*27, 1385-1390, doi:10.1016/0032-3861(86)90038-8 (1986).

23 Levita, G., Marchetti, A. & Lazzeri, A. Fracture of ultrafine calcium carbonate/polypropylene composites. *Polymer Composites*10, 39-43, doi:10.1002/pc.750100106 (1989).

24 Nicolais, L. & Nicodemo, L. The Effect of Particles Shape on Tensile Properties of Glassy Thermoplastic Composites. *International Journal of Polymeric Materials*3, 229-243, doi:10.1080/00914037408072354 (1974).

25 Nicolais, L. & Narkis, M. Stress-strain behavior of styrene-acrylonitrile/glass bead composites in the glassy region. *Polymer Engineering & Science*11, 194-199, doi:10.1002/pen.760110305 (1971).

26 Katz, H. S. & Milewski, J. V. *Handbook of fillers for plastics*. (Van Nostrand Reinhold Co., 1987).

27 Hu, C.-F., Su, W.-S. & Fang, W. Development of patterned carbon nanotubes on a 3D polymer substrate for the flexible tactile sensor application. *Journal of Micromechanics and Microengineering*21, 115012 (2011).

28 Kendall, K. Fracture of particulate filled polymers. *British Polymer Journal*10, 35-38, doi:10.1002/pi.4980100107 (1978).

29 Jancar, J. & Dibenedetto, A. T. Failure mechanics in ternary composites of polypropylene with inorganic fillers and elastomer inclusions. *Journal of Materials Science*30, 2438-2445, doi:10.1007/bf01184598 (1995).

30 Moloney, A., Kausch, H., Kaiser, T. & Beer, H. Parameters determining the strength and toughness of particulate filled epoxide resins. *Journal of Materials Science*22, 381-393, doi:10.1007/bf01160743 (1987).

31 White, E. F. T. Fracture behaviour of polymers. Edited by A. J. Kinloch and R. J. Young, Applied Science Publishers, London and New York, 1983. Pp xxv + 496, Price £30.00. ISBN 0853341869. *British Polymer Journal*16, 114-114, doi:10.1002/pi.4980160231 (1984).

32 Radford, K. C. The mechanical properties of an epoxy resin with a second phase dispersion. *Journal of Materials Science*6, 1286-1291, doi:10.1007/bf00552042 (1971).

33 Amdouni, N., Sautereau, H. & Gerard, J. F. Epoxy composites based on glass beads. II. Mechanical properties. *Journal of Applied Polymer Science*46, 1723-1735, doi:10.1002/app.1992.070461004 (1992).

34 Frogley, M. D., Ravich, D. & Wagner, H. D. Mechanical properties of carbon nanoparticle-reinforced elastomers. *Composites Science and Technology*63, 1647-1654, doi:10.1016/s0266-3538(03)00066-6 (2003).

35 Sabri, F. *et al.* Thin film surface treatments for lowering dust adhesion on Mars Rover calibration targets. *Advances in Space Research*41, 118-128, doi:10.1016/j.asr.2007.06.074 (2008).

36 Scholtens, B. E., Fesmire, J. E., Sass, J. P., Augustynowicz, S. D. & Heckle, K. W. CRYOGENIC THERMAL PERFORMANCE TESTING OF BULK-FILL AND AEROGEL INSULATION MATERIALS. *AIP Conference Proceedings*985, 152-159 (2008).

37 Guo, H. *et al.* Polyimide aerogels cross-linked through amine functionalized polyoligomeric silsesquioxane. *ACS Appl Mater Interfaces*3, 546-552, doi:10.1021/am101123h (2011).

38 Sabri, F. *et al.* Spectroscopic evaluation of polyurea crosslinked aerogels, as a substitute for RTV-based chromatic calibration targets for spacecraft. *Advances in Space Research*47, 419-427, doi:10.1016/j.asr.2010.09.014 (2011).

39 Goudie, J. L. & Collins, T. P. in *Electrical Insulation, 2004. Conference Record of the 2004 IEEE International Symposium on.* 475-479.

40 Goudie, J. L. & Collins, T. P. in Electrical Insulation, 2004. Conference Record of the 2004 IEEE International Symposium on. 475-479.

41 Moss, D. R. Pressure vessel design manual : illustrated procedures for solving major pressure vessel design problems. 3rd edn, (Gulf Professional Pub., 2004).

42 Bednar, H. H. Pressure vessel design handbook. 2nd edn, (Krieger Pub. Co., 1991).

43 Bickell, M. B. & Ruiz, C. Pressure vessel design and analysis. (Macmillan; St. Martin's P., 1967).

44 Spence, J. & Tooth, A. S. Pressure vessel design : concepts and principles. 1st edn, (E & FN Spon, 1994).

45 Annaratone, D. Pressure vessel design. (Springer, 2007).

46 Askeland, D. R., Fulay, P. P. & Wright, W. J. The science and engineering of materials. 6th edn, (Cengage Learning, 2011).

47 Meyers, M. A. & Chawla, K. K. Mechanical behavior of materials. 2nd edn, (Cambridge University Press, 2009).

48 Ghosh, P. Polymer science and technology: plastics, rubbers, blends and composites. (McGrawHill, 2001).

49 Bauman, J. T. Fatigue, stress, and strain of rubber components : a guide for design engineers. (Hanser Publications, 2008).

50 Gent, A. N. Engineering with rubber : how to design rubber components. 3rd edn, (Hanser Publishers, 2012).

51 Ferry, J. D. Viscoelastic properties of polymers. 3d edn, (Wiley, 1980).

52 Callister D., R. D. Materials Science and Engineering: An Introduction. 8 edn, (John Wiley and Sons, 2010).

53 Schneider F, F. T., J Wilde, and Wallarabe U. Mechanical properties of silicones for MEMS. Journal of Micromechanics and Microengineering 18, 065008, doi:10.1088/0960-1317/18/6/065008 (2008).

54 Meincke, O. et al. Mechanical properties and electrical conductivity of carbon-nanotube filled polyamide-6 and its blends with acrylonitrile/butadiene/styrene. Polymer 45, 739-748, doi:10.1016/j.polymer.2003.12.013 (2004).

55 Prisacariu, C. Polyurethane elastomers from morphology to mechanical aspects. (New York : Springer Verlag, 2011).

56 Boyce, M. C. & Arruda, E. M. An experimental and anaiytical investigation of the large strain compressive and tensile response of glassy polymers. Polymer Engineering & Science 30, 1288-1298, doi:10.1002/pen.760302005 (1990).

57 Ji, X. L., Jing, J. K., Jiang, W. & Jiang, B. Z. Tensile modulus of polymer nanocomposites. Polymer Engineering & Science 42, 983-993, doi:10.1002/pen.11007 (2002).

58 Douce, J., Boilot, J.-P., Biteau, J., Scodellaro, L. & Jimenez, A. Effect of filler size and surface condition of nano-sized silica particles in polysiloxane coatings. Thin Solid Films 466, 114-122, doi:10.1016/j.tsf.2004.03.024 (2004).

59 Wigley, D. A. Mechanical Properties of Materials at Low Temperature. First edn, (Plenum Press, 1971).

60 Semen B. Kharchenko1, Jack F. Douglas1, Jan Obrzut1, Eric A. Grulke2 and Kalman B. Migler1. Flow-induced properties of nanotube-filled polymer materialsNature Materials 3, 564 - 568 , doi:10.1038/nmat1183 (2004).

Appendix A

Properties of RTV 655:

Uncured Properties	Units	Properties
Color		Clear, colorless
Consistency		Easily pourable
Viscosity	mPa.s	5700
Specific gravity	g/cm^3	1.04

Uncured properties with curing agent added	Units	Properties
Mix ratio		10:1
color		Clear, colorless
Consistency		Easily pourable
Viscosity	mPa.s	5200
Work time @ 25^0C	Hrs	4

Cured Properties			
Mechanical	Tensile strength	MPa	6.5
	Elongation	%	120
	Shrinkage	%	0.2
Electrical	Refractive index		1.43
	Dielectric strength	kV/mm	19.7
	Dielectric constant @ 1 kHz		2.7
	Dissipation factor @ 1kHz		0.0004
	Volume resistivity	Ohm.cm	1.8×10^{15}
Thermal	Useful temperature range	^0C	-115 to 200
	Thermal conductivity	W/m.K	0.2
	Coefficient of expansion	m/m.K	33×10^{-5}
	Specific heat	J/g.K	1.3

Appendix B

Gas adsorption datasheet:

Date: 07/27/2011 Page 1

Quantachrome Corporation
Quantachrome Autosorb Automated Gas Sorption System Report
Autosorb for Windows® Version 1.19

Sample ID	Aerogel1				
Description	crosslinked aerogel powder, rifat				
Comments					
Sample Weight	0.0322 g				
Adsorbate	NITROGEN	Outgas Temp	130.0 °C	Operator	RF
Cross-Sec Area	16.2 Å²/molecule	Outgas Time	2.0 hrs	Analysis Time	60.2 min
NonIdeality	6.580E-05	P/Po Toler	2	End of Run	07/26/2011 17:45
Molecular Wt	28.0134 g/mol	Equil Time	3	File Name	RF072611.RAW
Station #	1	Bath Temp.	77.35		

MULTIPOINT BET

P/Po	Volume [cc/g] STP	1/(W((Po/P)-1))
1.0478e-01	14.3580	6.522E+00
1.5606e-01	16.3735	9.036E+00
2.0635e-01	18.1458	1.146E+01
2.5619e-01	19.8814	1.386E+01
3.0564e-01	21.8834	1.609E+01

Area = 7.060E+01 m²/g

Slope = 4.776E+01

Y - Intercept = 1.566E+00

Correlation Coefficient = 0.999888

C = 3.151E+01

Quantachrome Corporation
Quantachrome Autosorb Automated Gas Sorption System Report
Autosorb for Windows® Version 1.19

Sample ID	Aerogel1				
Description	crosslinked aerogel powder, rifat				
Comments					
Sample Weight	0.0322 g				
Adsorbate	NITROGEN	Outgas Temp	130.0 °C	Operator	RF
Cross-Sec Area	16.2 Å²/molecule	Outgas Time	2.0 hrs	Analysis Time	60.2 min
NonIdeality	6.580E-05	P/Po Toler	2	End of Run	07/26/2011 17:45
Molecular Wt	28.0134 g/mol	Equil Time	3	File Name	RF072611.RAW
Station #	1	Bath Temp.	77.35		

t-Method Micropore Analysis (de Boer)

P/Po	Thickness Å	Volume [cc/g] STP
1.0478e-01	3.71	14.358
1.5606e-01	4.08	16.373
2.0635e-01	4.41	18.146
2.5619e-01	4.73	19.881
3.0564e-01	5.05	21.883

Slope = 5.590E+00

Y - Intercept = -6.449E+00 cc/g

Micro-pore volume = 0.000E+00 cc/g

Micro-pore area = 0.000E+00 m²/g

External Surface Area = 7.060E+01 m²/g

Correlation Coefficient = 0.999586

Quantachrome Corporation
Quantachrome Autosorb Automated Gas Sorption System Report
Autosorb for Windows® Version 1.19

Sample ID	Aerogel1				
Description	crosslinked aerogel powder, rifat				
Comments					
Sample Weight	0.0322 g				
Adsorbate	NITROGEN	Outgas Temp	130.0 °C	Operator	RF
Cross-Sec Area	16.2 Å²/molecule	Outgas Time	2.0 hrs	Analysis Time	60.2 min
NonIdeality	6.580E-05	P/Po Toler	2	End of Run	07/26/2011 17:45
Molecular Wt	28.0134 g/mol	Equil Time	3	File Name	RF072611.RAW
Station #	1	Bath Temp.	77.35		

BJH ADSORPTION PORE SIZE DISTRIBUTION

Diameter Å	Pore Vol [cc/g]	Pore Surf Area [m²/g]	Dv(d) [cc/Å/g]	Ds(d) [m²/Å/g]	Dv(log d) [cc/g]	Ds(log d) [m²/g]
17.17	6.900E-03	1.608E+01	2.712E-03	6.321E+00	1.070E-01	2.494E+02
19.68	1.336E-02	2.921E+01	2.603E-03	5.292E+00	1.178E-01	2.395E+02
22.20	2.003E-02	4.122E+01	2.603E-03	4.691E+00	1.329E-01	2.395E+02
24.84	2.810E-02	5.422E+01	2.962E-03	4.769E+00	1.693E-01	2.725E+02

Quantachrome Corporation
Quantachrome Autosorb Automated Gas Sorption System Report
Autosorb for Windows® Version 1.19

Sample ID	Aerogel1				
Description	crosslinked aerogel powder, rifat				
Comments					
Sample Weight	0.0322 g				
Adsorbate	NITROGEN	Outgas Temp	130.0 °C	Operator	RF
Cross-Sec Area	16.2 Å²/molecule	Outgas Time	2.0 hrs	Analysis Time	60.2 min
NonIdeality	6.580E-05	P/Po Toler	2	End of Run	07/26/2011 17:45
Molecular Wt	28.0134 g/mol	Equil Time	3	File Name	RF072611.RAW
Station #	1	Bath Temp.	77.35		

SF Method Pore Size Distribution

Pore Width [Å]	Dv(w) [cc/Å/g]	Pore Width [Å]	Dv(w) [cc/Å/g]	Pore Width [Å]	Dv(w) [cc/Å/g]
3.5077	0.00000	7.3830	0.00000	11.2583	0.00002
3.6000	0.00000	7.4753	0.00000	11.3506	0.00002
3.6922	0.00000	7.5675	0.00000	11.4428	0.00002
3.7845	0.00000	7.6598	0.00000	11.5351	0.00002
3.8768	0.00000	7.7521	0.00000	11.6274	0.00002
3.9691	0.00000	7.8443	0.00000	11.7196	0.00002
4.0613	0.00000	7.9366	0.00000	11.8119	0.00002
4.1536	0.00000	8.0289	0.00000	11.9042	0.00002
4.2459	0.00000	8.1211	0.00000	11.9964	0.00003
4.3381	0.00000	8.2134	0.00000	12.0887	0.00003
4.4304	0.00000	8.3057	0.00000	12.1810	0.00003
4.5227	0.00000	8.3980	0.00000	12.2732	0.00003
4.6149	0.00000	8.4902	0.00000	12.3655	0.00003
4.7072	0.00000	8.5825	0.00000	12.4578	0.00003
4.7995	0.00000	8.6748	0.00000	12.5500	0.00003
4.8917	0.00000	8.7670	0.00000	12.6423	0.00004
4.9840	0.00000	8.8593	0.00000	12.7346	0.00004
5.0763	0.00000	8.9516	0.00000	12.8269	0.00004
5.1685	0.00000	9.0438	0.00000	12.9191	0.00004
5.2608	0.00000	9.1361	0.00000	13.0114	0.00004
5.3531	0.00000	9.2284	0.00000	13.1037	0.00004
5.4454	0.00000	9.3206	0.00000	13.1959	0.00005
5.5376	0.00000	9.4129	0.00000	13.2882	0.00005
5.6299	0.00000	9.5052	0.00000	13.3805	0.00005
5.7222	0.00000	9.5974	0.00000	13.4727	0.00005
5.8144	0.00000	9.6897	0.00000	13.5650	0.00005
5.9067	0.00000	9.7820	0.00001	13.6573	0.00006
5.9990	0.00000	9.8743	0.00001	13.7495	0.00006
6.0912	0.00000	9.9665	0.00001	13.8418	0.00006
6.1835	0.00000	10.0588	0.00001	13.9341	0.00006
6.2758	0.00000	10.1511	0.00001	14.0263	0.00007
6.3680	0.00000	10.2433	0.00001	14.1186	0.00007
6.4603	0.00000	10.3356	0.00001	14.2109	0.00007
6.5526	0.00000	10.4279	0.00001	14.3032	0.00007
6.6448	0.00000	10.5201	0.00001	14.3954	0.00007
6.7371	0.00000	10.6124	0.00001	14.4877	0.00008
6.8294	0.00000	10.7047	0.00001	14.5800	0.00008
6.9217	0.00000	10.7969	0.00001	14.6722	0.00008
7.0139	0.00000	10.8892	0.00001	14.7645	0.00008
7.1062	0.00000	10.9815	0.00001	14.8568	0.00009
7.1985	0.00000	11.0737	0.00001	14.9490	0.00009
7.2907	0.00000	11.1660	0.00002	15.0413	0.00009

Appendix C

293K tensile profile: 25 wt. % RTV-PCSA

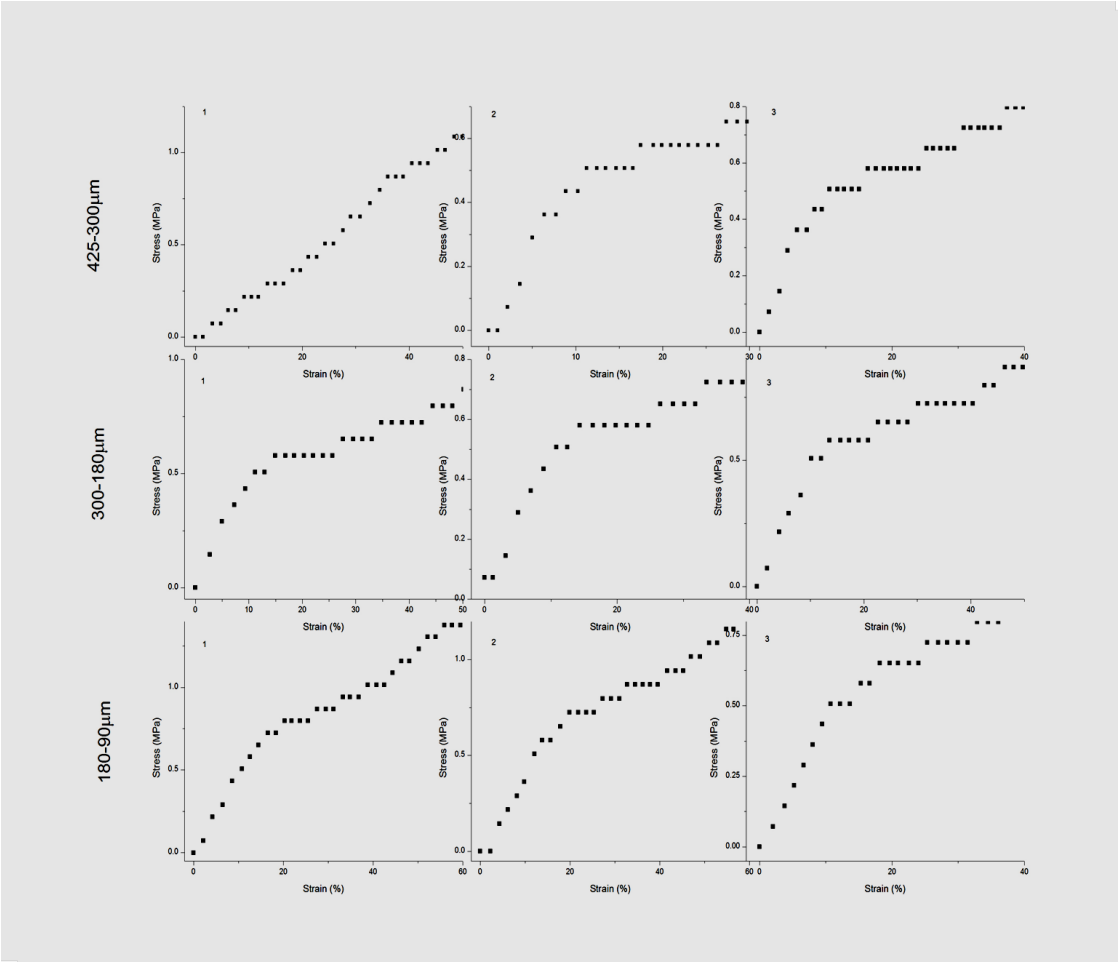

Figure A.1: Tensile profile of 25 wt. % impregnated compound samples at 293K. Samples are cured with the three differing set of compound samples are noted on the right side of the plots respectively. Each set contains three samples arranged from the left to right.

293K tensile profile: 50 wt. % impregnated RTV-PCSA

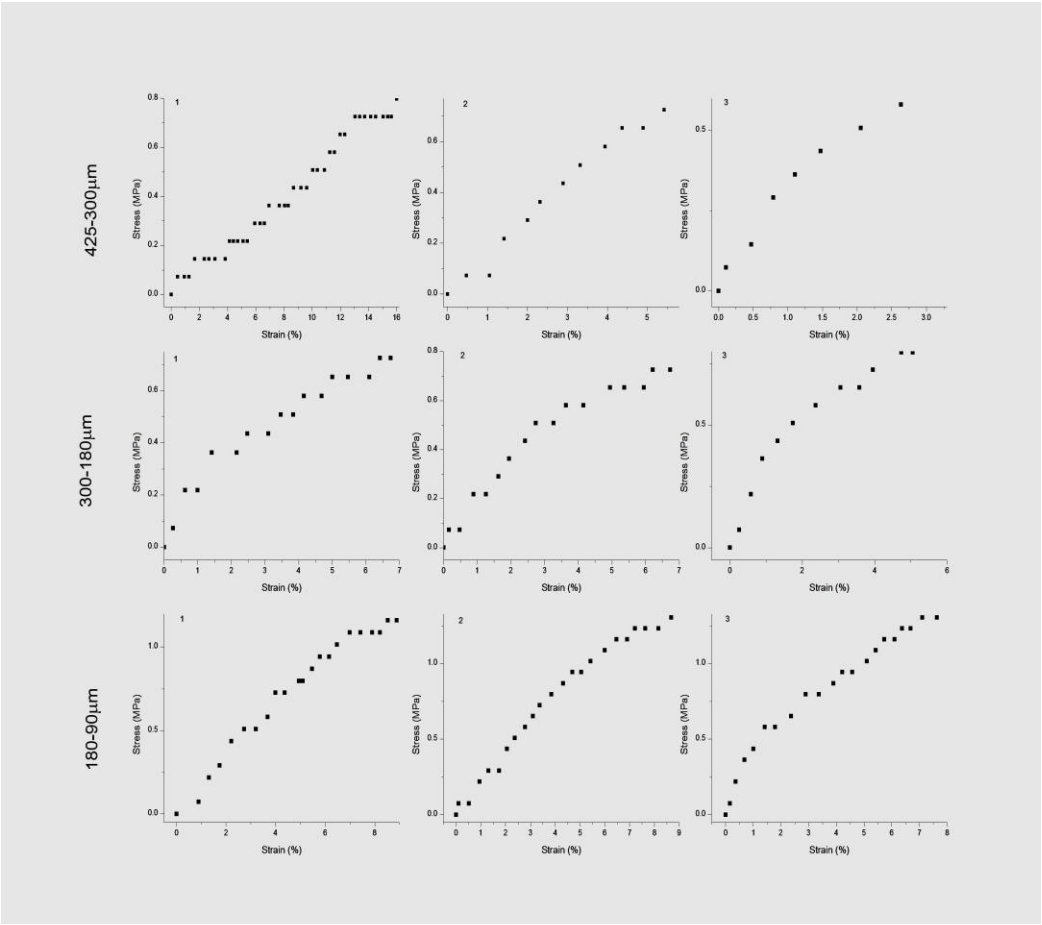

Figure A.2: Tensile profile of 50 wt. % impregnated compound samples at 293K. Samples are cured with the three differing set of compound samples are noted on the right side of the plots respectively. Each set contains three samples arranged from the left to right.

293K tensile profile: 75 wt. % RTV-PCSA

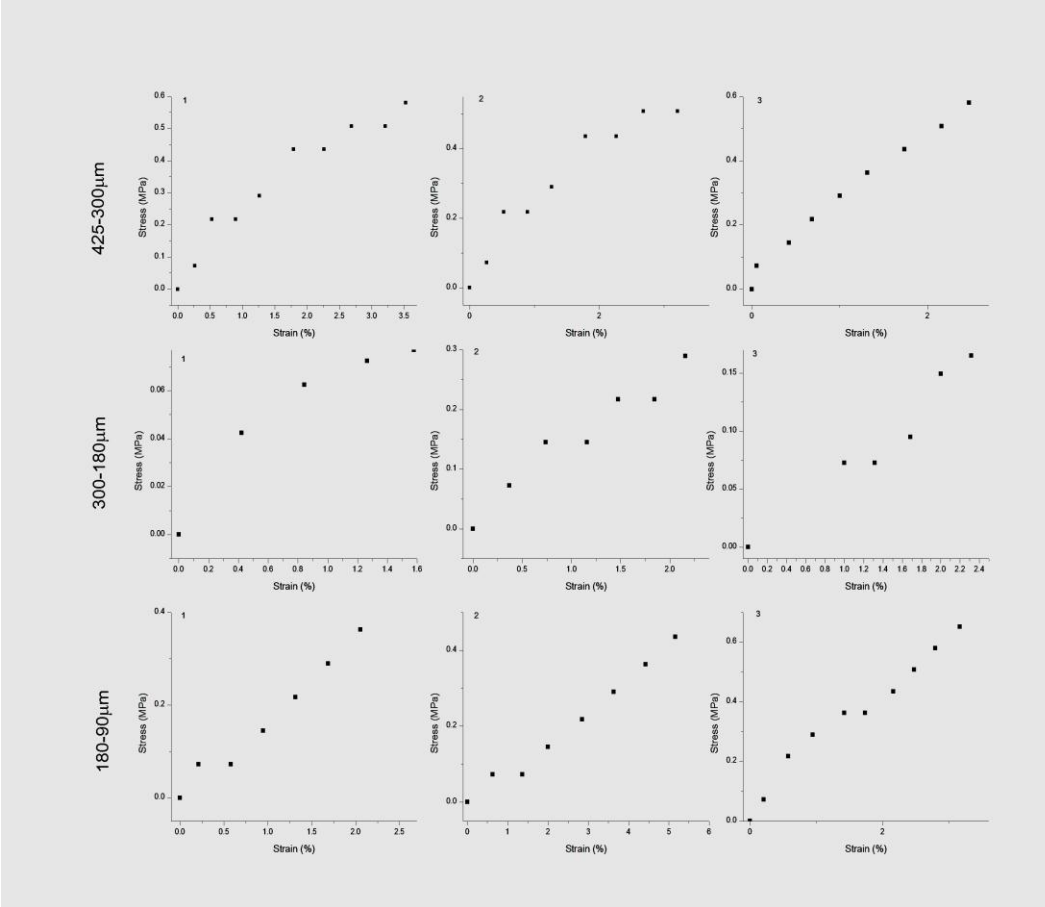

Figure A.3: Tensile profile of 75 wt. % impregnated compound samples at 293K. Samples are cured with the three differing set of compound samples are noted on the right side of the plots respectively. Each set contains three samples arranged from the left to right.

Appendix D

77K tensile behavior: 25 wt. % RTV-PCSA:

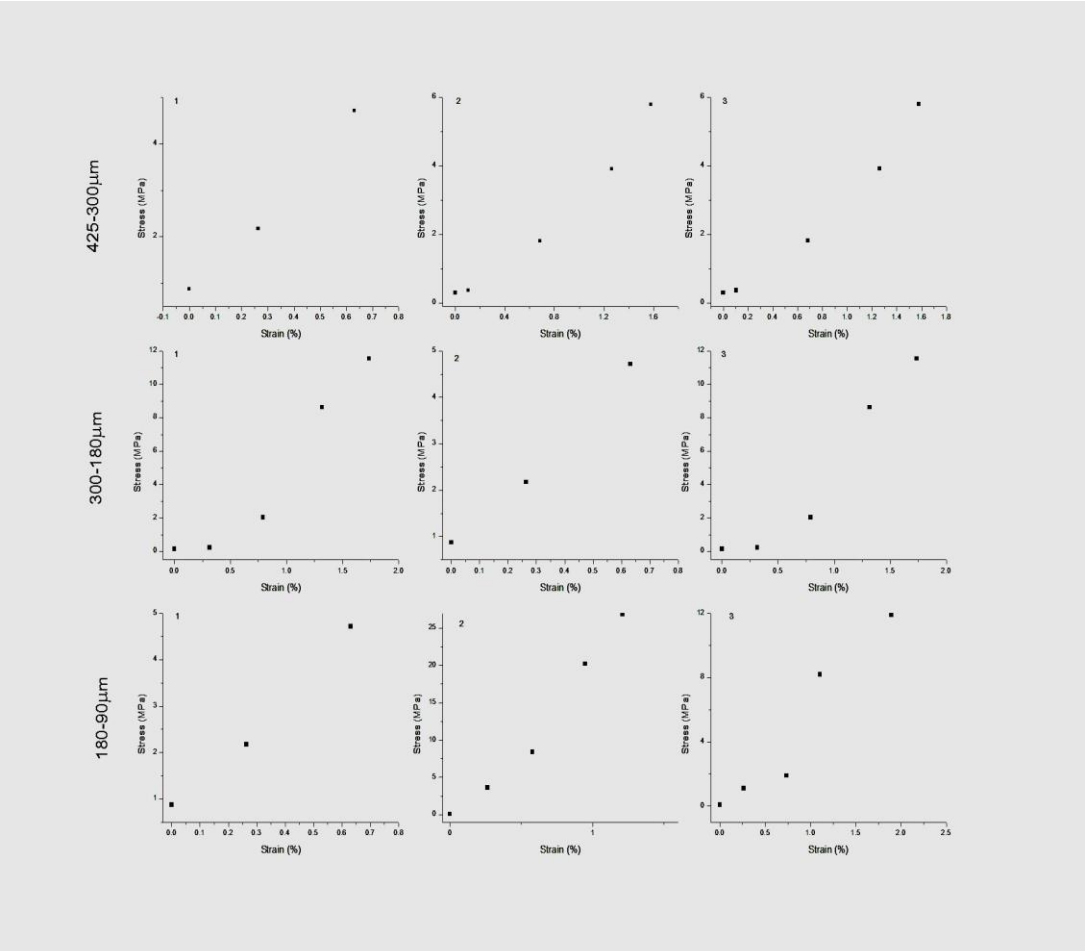

Figure A.3: Tensile profile of 25 wt. % impregnated compound samples at 77K. Samples are cured with the three differing set of compound samples are noted on the right side of the plots respectively. Each set contains three samples arranged from the left to right.

77K tensile behavior: 50 wt. % RTV-PCSA:

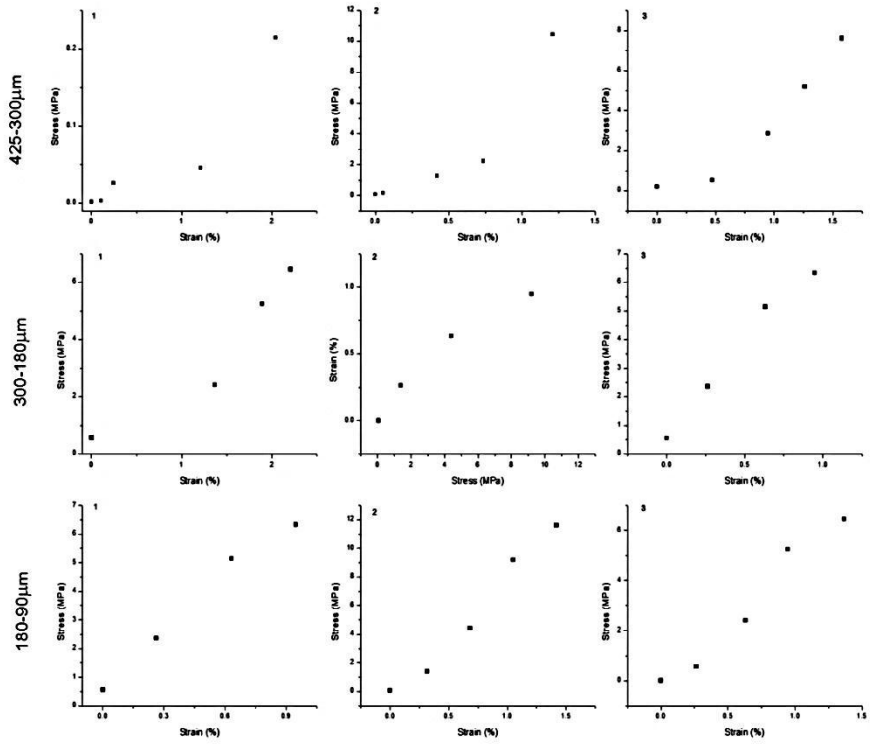

Figure A.4: Tensile profile of 50 wt. % impregnated compound samples at 77K. Samples are cured with the three differing set of compound samples are noted on the right side of the plots respectively. Each set contains three samples arranged from the left to right.

77K tensile behavior: 75 wt. % RTV-PCSA:

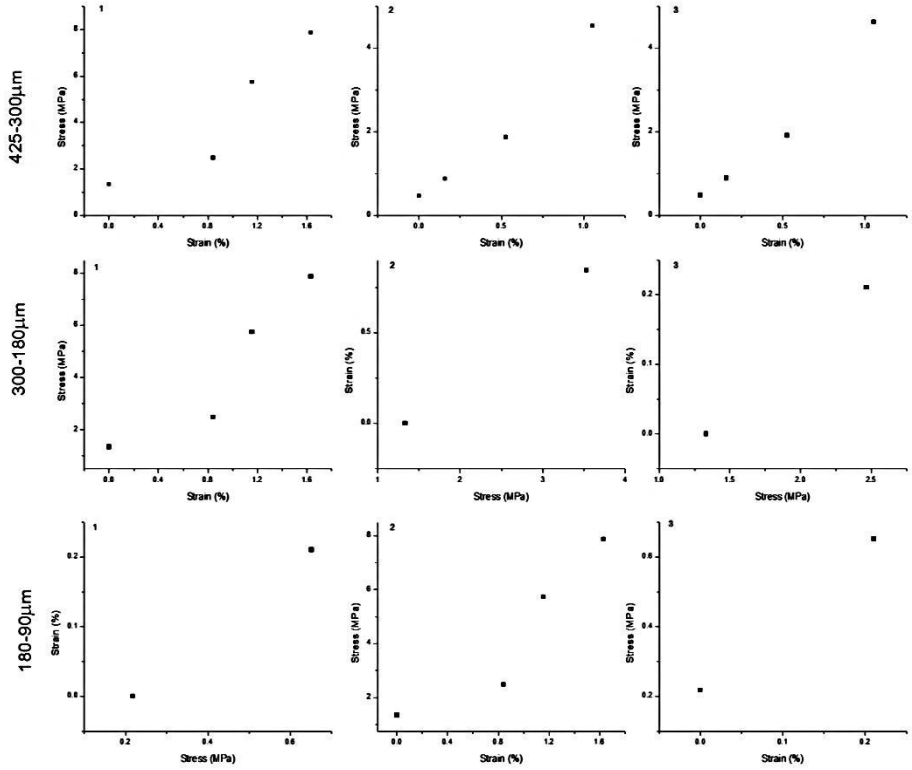

Figure A.5: Tensile profile of 75 wt. % impregnated compound samples at 77K. Samples are cured with the three differing set of compound samples are noted on the right side of the plots respectively. Each set contains three samples arranged from the left to right.